One-way Fluid-Structure Interaction of a Medium-Sized Heliostat using Scale-Resolving CFD Simulation

J.R.Wolmarans[1]and K.J. Craig[2]*

[1]Graduate student [2]PrEng, PhD, Professor

Department of Mechanical and Aeronautical Engineering, University of Pretoria, Pretoria 0002, South Africa.

*Tel.: +27-12-420-3515; E-mail address: ken.craig@up.ac.za. Corresponding author

Abstract. Vortex shedding and the resultant transient loadings on a medium-sized heliostat are investigated in this paper. Reynolds-Averaged Navier-Stokes (RANS) Computational Fluid Dynamics (CFD) of a simplified version of an operational heliostat, the LH-2, is used as a validation case for mean loads and to define the orientations used for fluid-structure interaction (FSI): maximum drag in the upright position, and maximum torque-tube moment at an elevation of 60° relative to the vertical. Optimized Atmospheric Boundary Layer profiles for mean flow and turbulence intensity were implemented as the inlet flow boundary condition for both the RANS and Stress-Blended Eddy Simulation (SBES) simulations, with the latter using the synthetic turbulence technique, the Vortex Method, at the inlet. The SBES results show a strong likeness to the experimental results of Peterka (1986) with a comparable mean and peak loading distribution. The transient SBES CFD pressure was implemented in a one-way FSI simulation to obtain the structural response of the heliostat to the transient wind loading. The results show that the response of the heliostat conformed to and depended on the mode shapes and frequencies of the heliostat structure more so than the vortex shedding frequencies. For the upright case, the Strouhal number obtained was within 8% of that obtained from an experimental study in literature, with the main vortex-shedding frequency shown to be 0.5 Hz. When excited with this wind, the structure responded with the third modal frequency of 2.7 Hz. The 60° elevation case also responded mainly with the third mode of 2.6 Hz being excited, but the response was significantly influenced by a combination of higher modes located around 6 Hz. The results from the transient structural analysis using the temporal SBES heliostat surface pressure fields as input indicate that the method holds promise in predicting the transient response of heliostats. Importantly it can be concluded that due to the difference in frequencies between the vortex shedding and modal frequencies, the structure is safe from self-excitation.

Keywords: Heliostat; Fluid-Structure Interaction (FSI); Stress-Blended Eddy-Simulation (SBES); Computational Fluid Dynamics (CFD); Atmospheric Boundary Layer (ABL)

Nomenclature

A_{REF}	*Reference Area (m^2)*	u_{Ref}	*Reference velocity (m/s)*
C_{DES}	*Constant for DES mesh*	u_p	*Mean velocity at cell centroid (m/s)*
C_s	*Smagorinsky constant*	$u(z)$	*Velocity (m/s)*
C_μ	*Turbulence modeling constant*	$\overline{U}(z)$	*Mean velocity (m/s)*

$u*$	*Friction velocity (m/s)*	*x,y*	*Streamwise and normal coordinates in CFD model (m)*
$Er(z_o)$	*Error*	y_p	*Distance to wall centroid (m)*
F_{SDES}	*Shielding function for SDES*	z	*General normal wall coordinate*
I_u	*Turbulence intensity(%)*	z_0	*Aerodynamic roughness length (m)*
k	*Turbulence kinetic energy (m^2/s^2)*	z_{Ref}	*Reference in height (m)*
K_s	*Equivalent sand grain roughness (m)*	*Greek Symbols*	
k-ε	*Turbulence model*	β^*	*Turbulence constant*
k-ω	*Turbulence Model*	Δ_{max}	*Cell volume (m^3)*
l_o	*Integral length scale (m)*	ε	*Dissipation rate (m^2/s^3)*
L_{REF}	*Reference length (m)*	κ	*Von Karman's constant*
L_t	*Integral length scale (m)*	μ	*Dynamic viscosity (kg/ms)*
$L_u^x(z)$	*Integral length scale (m)*	ξ	*Total number of data points*
N_s	*Number of samples*	ρ	*Density (kg/m^3)*
r	*Lag number*	σ_u^2	*Variance of velocity fluctuations*
R	*Autocorrelation function*	τ_{ij}^{SBES}	*Shear stress (Pa)*
Re	*Reynolds number*	τ_0	*Lag time (s)*
S	*Modulus of mean rate of strain tensor (s^{-1})*	φ	*Data point*
T_u^x	*Integral time scale (s)*	ω	*Specific dissipation (s^{-1})*

1. INTRODUCTION

Heliostat structures make up a large portion of the initial capital cost of a central receiver concentrating solar power plant due to the amount of heliostats needed, especially for medium-sized heliostats like the LH-2 used at Ivanpah (173 500) (Huss et al, 2011). The heliostat field can account for almost a third of the costs of a Concentrated Solar Power (CSP) tower plant. Improving the design of heliostats to be lighter, use less material and require smaller actuators would all be cost-reducing drivers. Wind loading is the main factor that may cause degradation in heliostat optical and structural performance and plant availability.

Heliostats are essentially bluff bodies and as such disturb the flow in a way as to generate oscillations that in turn interact with the structural components of the body (Bearman (1971, 1984), Chen and Chiou (1998), Cruz et al. (2008), Matty (1979), Sakamoto and Arie (1983). Of interest is how the turbulent spectrum of the attacking wind interacts with the vortex-shedding of the bluff body, and which of these flow-excitation phenomena cause excitation of the modes of the structure.

Previous studies have been performed to estimate wind-loading effects on heliostats. Reviews were provided by Sun et al. (2014) and Pfahl et al. (2017), whereas Pfahl et al. (2011a, 2011b) considered the effects of aspect ratios and Reynolds numbers. Various researchers have quantified the modal frequencies and mode shapes of heliostats (e.g., Griffith et al. (2015), Vásques-Arango et al. (2015))

and found lowest modal frequencies on the order of 1.6 to 3 Hz. Gong et al. (2012) investigated the wind-induced dynamic response of a heliostat experimentally in a wind tunnel and also focused on the heliostat pressure distribution characteristics (Gong et al., 2013). The effect of wind on heliostats operating in a field was considered by Sment and Ho (2014). Here the effect of the field configuration is for the outer row of heliostats to shield downstream heliostats that are in tandem (Sakamoto et al. (1987), Yu et al. (2016), Emes et al. (2017)). The current work focuses on a single heliostat as a worst-case approximation of the outer row behavior.

What complicates the study of heliostat aerodynamics is that the fact that they are active pieces of hardware, their function in reflecting the sun's solar radiation requires that they constantly track the sun's position with movement about at least two axes. The angle of the mirror constantly changes throughout the day; this leads to varying wind loads on the heliostat, coupled with the individual heliostat's placement in the field, creates fluctuating conditions that need to be designed for. For optimal operation the heliostats are required to be as stiff as possible, both statically and dynamically.

The fact that the heliostats have to face the natural elements, particularly wind, makes their design a highly complex task. Here, much can be learnt from previous studies on wind loading of building structures (e.g., Cook (1985), Dyrbye and Hansen (1996), Holmes et al. (2012)). An insight into the complete load evaluation process of a heliostat is given for the SENER heliostat by Rebolo et al. (2011). Wind codes are combined with wind tunnel tests, CFD analysis, structural analysis and field measurements to prove the design. Atmospheric Boundary Layer (ABL) modeling is needed to try and replicate the conditions experienced by the heliostats on the ground. ABL modeling is in itself a complicated area of science and numerous papers exist detailing the best approaches that should be used when modeling this in Computational Fluid Dynamics (CFD). Many factors can influence the models such as boundary and inlet conditions, and the nature of wind loading is in itself stochastic (Deaves and Harris, 1978). This leads to the problem of over and under-design of the heliostats, over-design due to the poor prediction of the wind loads means that the heliostat structures are larger than they need to be and ultimately more expensive than they should be. Under-design is just as much of an issue as this would lead to the inevitable failure of the heliostat before its designed lifespan, causing excessive maintenance costs and possibly the closure of an operational plant.

When refining heliostat designs, fluid-structure interaction (FSI) becomes more important and needs to be well understood to assess its affect. FSI is well established in other fields of science and engineering (see, e.g., Bungartz and Schafer (2006)), but there is limited work done on heliostats, with a notable exception being Vásques-Arango (2016), who combined LES with a transient finite element simulation and an admittance method to determine the statistical response of the structure. The current work hopes to compliment that study by using a more cost-effective hybrid RANS-LES implementation in the form of the Stress-Blended Eddy Simulation (SBES) method.

It is the objective of this study to illustrate the use of FSI in the evaluation of aerodynamic and structural performance for a medium-sized heliostat. Coupled, or two-way FSI, using LES-type CFD is still too costly, hence, to reach this goal, this study proposes a one-way coupling of ANSYS Fluent CFD and ANSYS Mechanical Finite Element Analysis (FEA) on a simplified version of the LH-2 heliostat, seen in Figure 1, hereafter called "the heliostat". Sub-objectives are, to firstly characterize the ABL and, secondly, to model the flow over the heliostat comparing Reynolds-Averaged Navier-Stokes (RANS) CFD against validation data from the Huss et al. (2011) experiment. By determining the mean loads, two orientations are identified for fluid-structure interaction (FSI): maximum drag in the upright position, and maximum torque-tube moment at an elevation of 60° relative to the vertical. The next sub-objective is to perform a Stress-Blended Eddy Simulation (SBES) Scale-Resolving Simulation (SRS) CFD simulation of the heliostat for these two orientations. Finally, a one-way FSI employing the SBES temporal surface pressure contours is presented and discussed. Conclusions and future work suggestions end the paper.

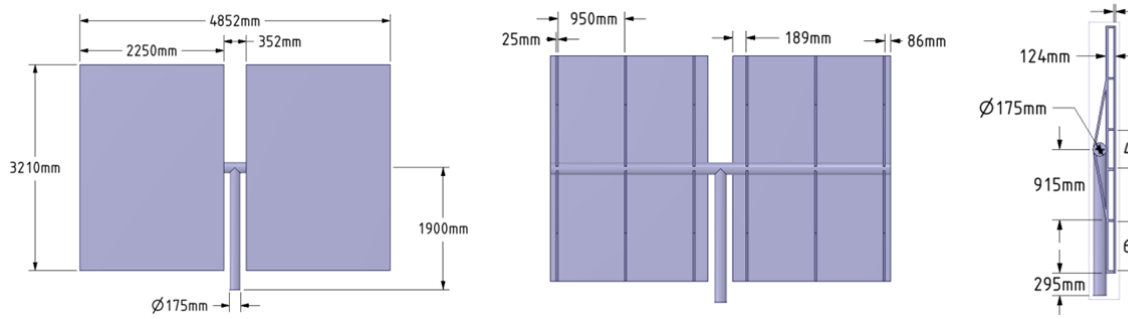

Figure 1. Computational model of the full-scale heliostat. The CFD model does not include the support braces on the right figure. The structural model does include the braces.

2. METHODOLOGY

The first step in accurately modeling the flow over a heliostat is correctly characterizing the ABL. Blocken et al. (2007) and Richards and Norris (2011) provide guidelines for the correct modeling of the ABL. Blocken et al. (2007) stress the need for a horizontally homogeneous ABL in the computational domain, this means that in the vertical profiles of the mean velocity and turbulence there is an absence of streamwise gradients. This will occur when the mean velocity and turbulence profiles are in equilibrium with the roughness characteristics of the ground surface (Blocken et al. 2007). Blocken et al. (2007) describes four requirements that need to be simultaneously satisfied if the wall roughness is expressed by an equivalent sand grain roughness in the wall functions which is the case here. They are:

1. A sufficiently high mesh resolution in the vertical direction close to the bottom of the computational domain.
2. A horizontally homogeneous ABL flow in the upstream and downstream region of the domain.
3. A distance y_p from the centre point P of the wall adjacent cell to the wall that is larger than the physical roughness height K_s of the terrain. (No longer needed due to software advances)
4. Knowing the relationship between the equivalent sand grain roughness height and the corresponding aerodynamic roughness length z_0.

Once the ABL is modeled correctly, the mean flow over the heliostat can be modeled with confidence using Reynolds-Averaged Navier-Stokes (RANS) CFD, here using either the Realizable k-ε (RKE) and Shear-Stress Transport (SST) k-ω turbulence models. A modal analysis is performed on the full-scale 3D heliostat in order to investigate the frequencies that may be of concern with regards to vortex shedding and transient peak loadings. To resolve peak loadings, Scale-resolving CFD is implemented using the Stress-Blended Eddy Simulation (SBES) model, a hybrid model that utilises both RANS and Large Eddy Simulation (LES) capabilities. The wall bounded flow is modeled with the SST k-ω model while the main turbulence features of the flow are resolved with LES. This is used in order to assess the peak loadings on the heliostat due to the vortex shedding which cannot be modeled using URANS. The pressure field developed on the heliostat structure is transferred to ANSYS Mechanical where a transient structural analysis is performed.

3. PRECURSOR RANS SIMULATION AND VALIDATION

In order to perform accurate CFD simulations on the heliostat, the ABL needs to be correctly modeled. A physical roughness height needs to be computed to ensure horizontal homogeneity of the inlet ABL. The relationship between the physical roughness height and the aerodynamic roughness for the fully rough regime can be derived by first-order continuity fitting of the ABL log law and the wall-function log law including the appropriate roughness function at height $z = z_0$. Based on the data by Cebeci and Bradshaw (1977) this relationship is given as:

$$K_S = \frac{9.793 z_0}{C_S} \tag{1}$$

To characterize the ABL, the Peterka (1986) profiles for the mean velocity and turbulence intensity are used. These profiles are used inthe proceeding CFD validation done on the wind tunnel experiment of Peterka (1986). The first step in modeling the ABL is to ensure the equations for the velocity profile are arranged in the correct manner as seen in equation 2 to find the friction velocity u* for a given reference velocity, u_{Ref}, at a certain reference height, z_{Ref}.

$$u^* = \frac{u_{Ref}\kappa}{\ln\left(\frac{z_{Ref}}{z_o}\right)} \tag{2}$$

The normalized velocity profile may be attained using equation 2:

$$\frac{u(z)}{u_{Ref}} = \frac{\ln\left(\frac{z}{z_o}\right)}{\ln\left(\frac{z_{Ref}}{z_o}\right)} \tag{3}$$

where

$u(z) = Streamwise\ velocity\ component\ at\ height\ z\left[\frac{m}{s}\right]$
$z = Height\ above\ groundplane\ [m]$
$u_p = Mean\ velocity\ at\ wall\ adjacent\ cell\ centroid\left[\frac{m}{s}\right]$
$\kappa = von\ Karman's\ constant$

Applying the boundary conditions of Richards and Hoxey (1993), the only value that can be altered to match a given velocity profile is that of the aerodynamic roughness z_o. Using equation 3, a fitted curve is obtained to match the mean velocity profile (here using the data of Peterka (1986)). A least-squares minimization problem is solved using equation 4 in MATLAB to find the aerodynamic roughness that gives the best fit for the mean velocity profile.

$$Er(z_o) = \sum_{\varphi=1}^{\xi}\left[U_\eta - U_{Ref}\frac{\ln\left(\frac{z}{z_o}\right)}{\ln\left(\frac{z_{Ref}}{z_o}\right)}\right]^2 \tag{4}$$

where:
$Er(z_o) = Sum\ of\ the\ squared\ error$
$\varphi = Experimental\ data\ point$
$\xi = Total\ number\ of\ experimental\ data\ points$

The result of equation 4 provides an aerodynamic roughness constant that will optimally match the velocity profile of Peterka (1986) to that of the simulation. Unfortunately, in ANSYS Fluent it is not possible to specify a turbulence intensity profile, rather k and ε have to be specified at the inlet. From the definition of k and the assumption of isotropic turbulence, we can relate the turbulence intensity I_u to k as shown in equation 5:

$$I_u(z) = \frac{\sqrt{\overline{u'^2}}}{u(z)} = \frac{\sqrt{\frac{2}{3}k}}{u(z)} \tag{5}$$

Looking at equation 5, there is no way to control the turbulence intensity profile after the velocity profile has been determined. It can be concluded that the turbulence intensity profile is a direct

consequence of the velocity profile. A form for the optimization via least squares is obtained to find the aerodynamic roughness constant that will provide the best profile fit to the Peterka (1986) turbulence intensity profile. Applying an aerodynamic roughness constant that best fits the turbulence intensity means the mean velocity profile is no longer an optimum fit to Peterka (1986). Using Equation 3 to model the mean velocity profile allows for the reference height to be changed along with the reference velocity at that specific height. This means that the velocity profile can still match the Peterka (1986) profile at the areas of interest while having a more accurate accompanying turbulence intensity profile. This is a better means of modeling the ABL flow as the drag coefficient and subsequent fluctuations are highly sensitive to the turbulence. The least-squares minimization problem solved in MATLAB to find the aerodynamic roughness that gives the best fit for the turbulence intensity profile is displayed in equation 6.

$$Er(z_o) = \sum_{\eta=1}^{\xi} \left[I_{u\eta} - \frac{\sqrt{\left(\frac{2}{3}\right)\left(\frac{u_{Ref}\kappa}{\ln\left(\frac{z_{Ref}+z_o}{z_o}\right)}\right)^2}}{\frac{(\sqrt{C_u})}{U_{Ref}\frac{\ln\left(\frac{z}{z_o}\right)}{\ln\left(\frac{z_{Ref}}{z_o}\right)}}} \right]^2 \quad (6)$$

The results of the Peterka (1986) MATLAB profile optimization can be seen in Fig.2A and B for the mean velocity and turbulence intensity profiles, respectively. In Fig.2A the profiles are given for an aerodynamic roughness z_o that optimizes the velocity profile. In Fig.2B the profiles are given for an aerodynamic roughness z_o that optimizes the turbulence intensity profile.

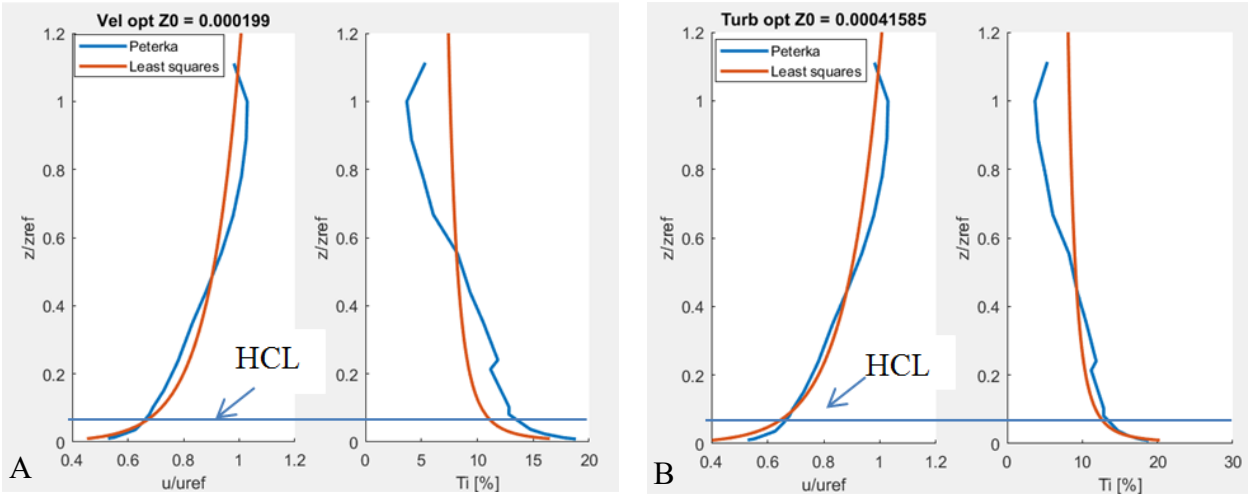

Figure 2. A) Optimized profiles (velocity),B) Optimized profiles (turbulence intensity), both compared with Peterka (1986).

The aerodynamic roughness z_o that optimizes the turbulence intensity profile produces a 3 percentage point reduction in the drag coefficient error compared to the velocity optimized profile. The turbulence intensity optimized profile is therefore used in the characterization of the ABL. The heliostat validation case performed in this study is the experiment of the LH-2 heliostat (Huss et al., 2011). The wind tunnel model used in the experiments is a 1:7 scale model of the LH-2. No inlet flow profiles are provided but the turbulent intensity is specified at a height of 0.2714m (equivalent to full-scale value of 1.9 m) for the longitudinal intensity of $I_u = 20\%$ while the intensity in the vertical direction is $I_w = 12\%$. As no inlet profiles are specified, the ABL inlet profiles from Peterka (1986), are specified as inlet boundary

conditions for this case as a proxy (see domain and boundary conditions in Fig.3). The turbulence intensity in Fig.2B is altered by changing the aerodynamic roughness length, z_o, to match the 20% at the reference height of 0.2714 m (1.9 m full scale). The optimized z_o that resulted in $I_u = 20\%$ was found to be $z_o = 0.0107615$ m. The reference velocity of 10.5 m/s at a reference height of 10m full-scale (1.4286 m at scale) results in a Reynolds number of approximately Re = 500 000, which should ensure Reynolds number independence of the flow. Using a scale of 1:7, the resulting reference area is 0.3028 m^2 with the Heliostat Centre-Line (HCL) height being 0.2714 m.

A hybrid tetrahedral-hexahedral mesh is used. The mesh contains roughly 5 million cells with the cell size on the heliostat surface specified at a maximum of 3 mm. A close-up of the heliostat mesh can be seen in Fig.4. Increasing the mesh to about 30 million cells by refining the wake region, resulted in a difference of less than 1% for all monitored quantities in Fig.5 for the 60° case, for example. The 5 million cell mesh settings were therefore used for all elevation angles.

The RKE RANS equation is used for this simulation with standard wall functions. The double precision, SIMPLE solver is used with second-order spatial discretization schemes. The reference values used in Fluent are listed in Table 1. The steady-state flow field is assumed to be converged when the drag coefficient residual monitor reaches a value of $1x10^{-6}$ or the residuals reach a value of $1x10^{-6}$.

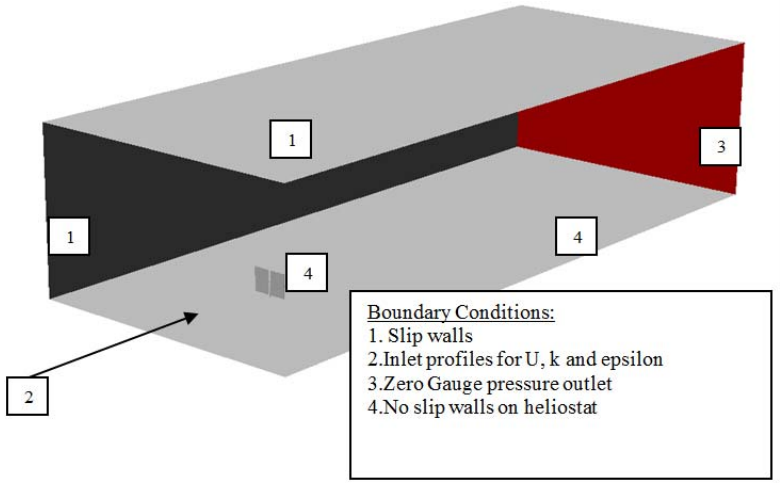

Figure 3. Computational domain and boundary conditions for heliostat validation. Upright heliostat configuration shown. Domain size (32.7H × 13.1H × 7.63H, H = 0.45857 m for 1:7 scale)

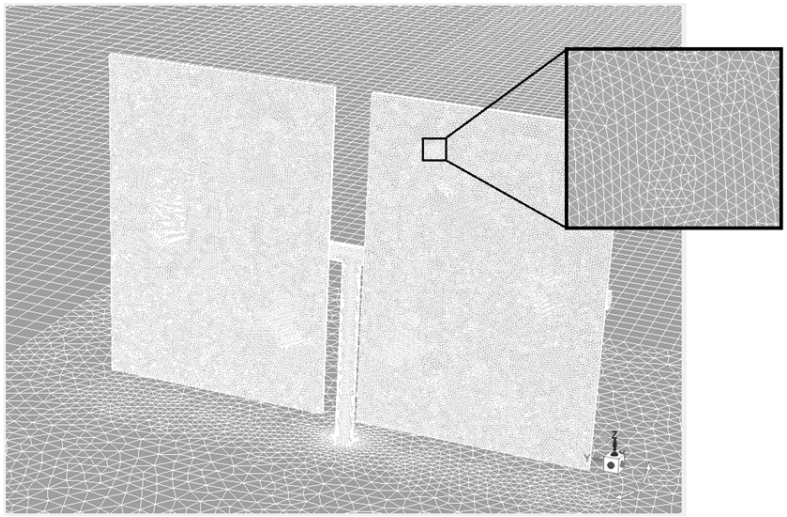

Figure 4. Close up view of the tetrahedral mesh on the heliostat surface. Upright heliostat configuration.

A_{REF}	0.3028 m^2
L_{REF}	0.2714 m
u_{REF}	10.5 m/s
ρ	1.225 kg/m^3
μ	1.7894×10^{-5} kg/ms

Table 1. Reference values and material properties used in ANSYS Fluent.

For this validation, the heliostat was positioned with the flow approaching normal to the mirror faces. The angle of the mirrors around the torque tube was parameterized and a parametric study was performed in ANSYS Workbench. Seven simulations were performed with the mirror being rotated around the torque-tube (elevation angle) starting at 0° (upright) and increasing in increments of 15° up to the final position of 90° (the stow position) for an azimuth angle of 0°. For all seven simulations, the drag, lift, pylon moment and torque tube moment coefficients were solved for, Fig.5. The coefficients were calculated by dividing the respective force by the dynamic pressure and the reference area (calculated using Tab.1 values), and for the moments, by the reference length, as well. These coefficients are compared to the wind tunnel results as well as the CFD results of Huss et al. (2011). The pylon moment is defined as the moment of the entire heliostat about the ground plane through the pylon. The torque tube moment is the moment created by the mirrors about the torque tube axis.

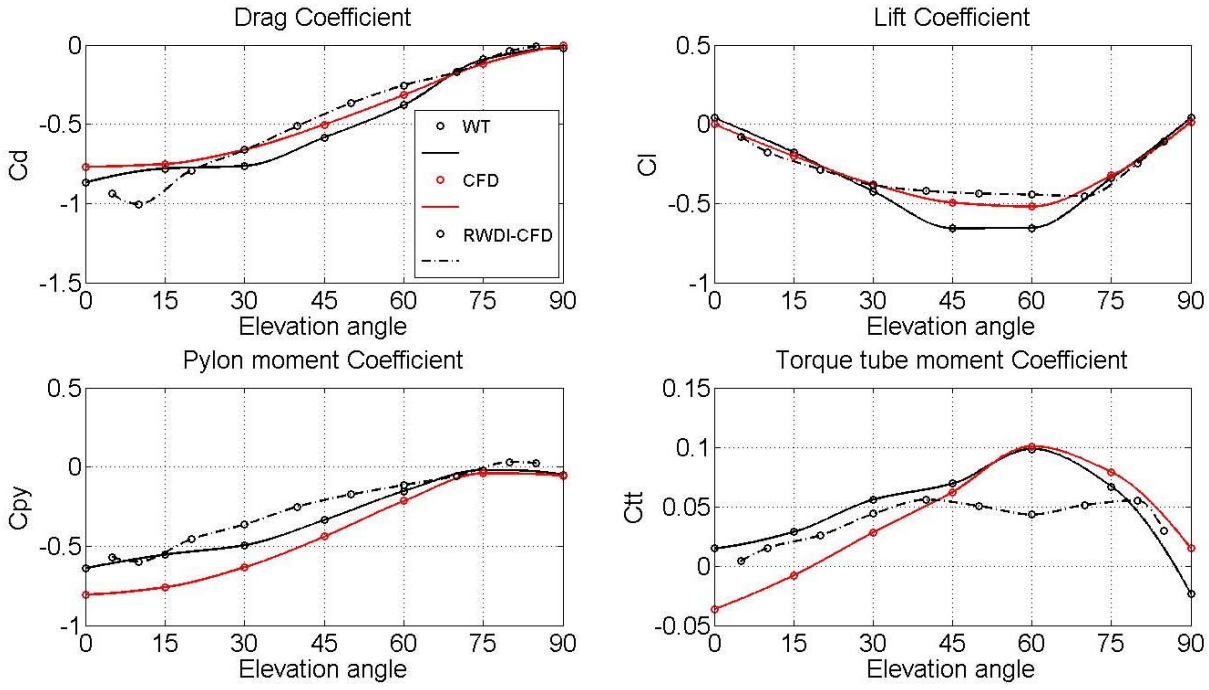

Figure 5. Aerodynamic coefficients obtained with RANS compared to the results of Huss et al. (2011) (RWDI-CFD = CFD resuls from RWDI reported in Huss et al. (2011)). Azimuth angle = 0°

The RKE RANS simulations produce results that are in close agreement with both the wind tunnel and CFD results of Huss et al. (2011). The current RANS CFD results in general outperform the RANS results reported in Huss et al. (2011). RANS simulations however only provide mean forces and moments and are such are not useful for fluid-structure interaction purposes, the focus of this paper.

The trends in Fig.5 are however useful for identifying representative heliostat orientations for further investigation. In the current study, these are the maximum drag case (upright (0°) angle), and the maximum torque-tube moment case (at 60° elevation angle).

SRS methods are required in order to resolve the major transient flow features present not only in the ABL but for those generated by the interaction of the ABL with the heliostat. These flow features are critical in simulating the transient response of the heliostat. They are required in order to determine if the heliostat undergoes harmonic resonance, leading to structural failure due either to the vortex shedding of the flow or simply from the frequency content of the turbulence already present in the ABL. This approach is described in the following section.

4. SCALE-RESOLVING SIMULATIONS

4.1 Implementation

The SBES SRS model is implemented in this work. It is a hybrid LES-RANS model, meaning it uses both RANS and LES modeling and conveniently switches between the two based on the comparison between the turbulent length scales and grid spacing. The SBES model evolved from the Detached Eddy Simulation (DES) and Shielded DES (SDES) models (ANSYS, 2018). The LES mode is activated once the model determines that the grid spacing in the areas of turbulent interest is the minimum. This can be seen in equation 7 with the regular RANS dissipation and the adjusted dissipation:

$$\varepsilon = \frac{k^{\frac{3}{2}}}{L_t} \rightarrow \varepsilon = \frac{k^{\frac{3}{2}}}{\min(L_t, C_{DES}\Delta_{max})} \tag{7}$$

The dissipation then takes the form of equation 8 with the shielding function described in equation 9:

$$\varepsilon_{SDES} = -\beta^* \rho \omega F_{SDES} \tag{8}$$

with

$$F_{SDES} = \left[\max\left(\frac{L_t}{C_{SDES}\Delta_{SDES}}(1 - f_{SDES}), 1\right) - 1\right] \tag{9}$$

When SDES switches to LES mode, the eddy viscosity is lowered to that of a conventional LES model:

$$\nu_t = ((\frac{\beta}{\alpha})^{\frac{3}{4}} C_{LES}\Delta)^2 S \tag{10}$$

The only other change lies with the LES length scale, in the DES models the length scale is problematic due to overly high levels of eddy viscosity in separating shear layers due to high aspect ratio cells normally found there. To avoid the issue of a slow transition from RANS to LES, the SDES model uses equation 11 for the LES length scale formulation, the first part of the equation is the normal cell volume and the second part ensures a limit for high aspect ratio cells:

$$\Delta_{SDES} = \max(\sqrt[3]{V}, 0.2\Delta_{max}) \tag{11}$$

The SBES model utilizes the same shielding function as the SDES model, but adds the ability to switch from the underlying RANS model directly to the LES model. The stress blending between the RANS and LES formulations is as follows:

$$\tau_{ij}^{SBES} = f_{SDES}\tau_{ij}^{RANS} + (1 - f_{SDES})\tau_{ij}^{LES} \tag{12}$$

The advantages of the SBES model are that you can generically combine LES and RANS models, clearly distinguish between RANS and LES regions based on the shielding function and utilize rapid transition from RANS to LES in separated shear layers. SBES provides the quickest transition from RANS to LES structures.

4.2 Precursor RANS simulation

The first step in conducting an accurate SBES simulation is performing a precursor RANS simulation. According to Menter (2015) if the RANS simulation provides a meaningful solution then the main quantity of relevance when it comes to the suitability of the mesh in the LES region is the ratio between the integral length scale and the grid size. The equations for the integral length scale, the grid size and the ratio are as follows:

$$l_o = \frac{k^{0.5}}{C_\mu \omega} = \frac{k^{1.5}}{\varepsilon}; \quad \Delta = \sqrt[3]{CellVolume} \quad ; \quad R = \frac{l_o}{\Delta} \tag{13}$$

According to Gerasimov (2016), a ratio of R = 12.5 translates to approximately 90% of turbulent kinetic energy being resolved. When this ratio is plotted over the entire domain, areas where the ratio is lower than 12.5 indicate a mesh that is too coarse for that particular area in order to resolve up to 90% of the turbulence. In other words, a low ratio area (<12.5) in the mesh equates to a mesh region that could be refined before the SRS simulation is conducted. This ratio equates to having approximately 10-12 cells across a length scale to warrant 90% resolution. It should be noted that the equation used to obtain the cell size is a crude estimate and thus the ratio used here gives a rough but useful insight into the suitability of the mesh for SBES. Aiming for a 90% resolution of the turbulence is a fair goal. This is due to the bulk of the turbulent structures of importance, that exhibit anisotropic behavior and influence the flow and structure the most, are resolved well before this point.

Two levels of mesh refinement were used in the SRS simulations. The coarse mesh used for the precursor RANS on a full-scale heliostat is a block-structured mesh having approximately 4.3 million cells. The fine mesh used is a regionally adapted version of the coarse mesh where the area around the heliostat extending into the wake is adapted with the final mesh containing approximately 27.8 million cells. The major difference between the precursor RANS performed for the SBES simulations and the RANS performed for the validation in Fig.5 is the switch to SST k-ω as RANS turbulence model. This thus becomes the underlying RANS model in the SBES model implemented in this section. The inlet has specified inlet velocity, turbulent kinetic energy and specific dissipation rate profiles prescribed via a User-defined function (UDF) so as to model the ABL as noted in previous section, but now at full scale (HCL = 1.9m).

The mesh used in the RANS validation simulations is also used as a comparison mesh in the proceeding sections for the results. No mesh refinement is performed allowing a clearly visible determination of the difference the mesh refinement used for the SRS results can produce. In the following sections the RANS validation mesh is referred to as the ‘coarse’ mesh and the refined adapted mesh as the ‘fine’ mesh.

The Courant-Friedrichs-Lewy (CFL) number is defined in equation 14. The temporal resolution should match or exceed the spatial resolution. Good practice to account for the differences between instantaneous and averaged velocities as well as for the errors introduced from RANS, is to use a CFL number of 0.5 or less.

$$CourantNumber = \frac{U\Delta t}{\sqrt[3]{CellVolume}} \leq 0.5 \tag{14}$$

To illustrate how the automatic separation between the LES (SBES) and RANS zones occur during the computation, Fig.6 shows a plot of the SBES shielding function, confirming that the RANS zone is confined to the region of the ground and on the heliostat (function = 1), with LES being applied elsewhere (function = 0).

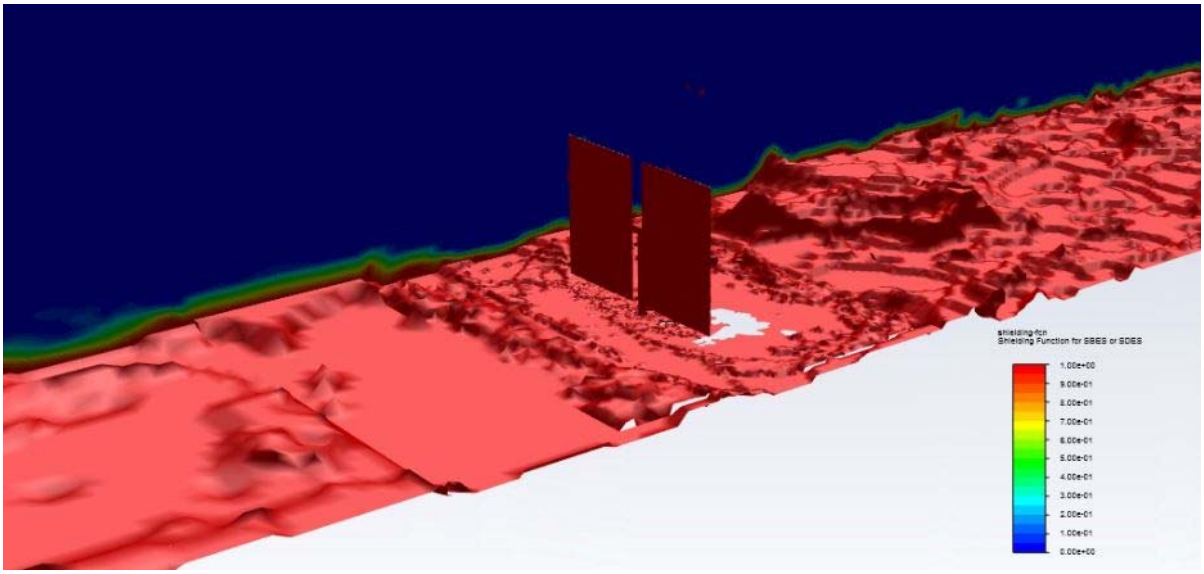

Figure 6. SBES shielding function iso-surface of 1 and contours at y=-5m: 0 indicates LES region and 1 indicates RANS region (0 degree orientation, fine mesh, time = 19.525 sec)

4.3 Turbulence spectrum and integral length scale

The time step used in the refined mesh SBES simulation is 0.0003 s. The vortex method is implemented in order to generate the synthetic turbulence in the form of velocity perturbations that are added at the inlet of the domain. As stipulated by Gerasimov (2016), the number of vortices prescribed should provide for approximately four vortices for every four cells on the inlet face, being 1825 in the current study. The SIMPLEC pressure-velocity coupling scheme is employed. The settings for the spatial discretisation are changed from the usual RANS settings implemented previously. Bounded Central Differencing (BCD) is used for the momentum discretisation with the Bounded Second-Order Implicit transient formulation used along with higher-order term relaxation. The sub-grid scale LES model used in the SBES simulation is the WALE model. The sub-grid scale stresses from the filtering operation are unknown and need to be modeled. In ANSYS Fluent the sub-grid scale models employ the Boussinesq hypothesis similarly to the RANS models. The benefit of SRS modeling is the ability to resolve the turbulence spectrum to a limit defined by the grid size. The energy cascade present in turbulent flows, describes how the larger eddies have an anisotropic nature. This makes it important for them to be resolved as they are normally the structures that play the most significant role in the fluid flow in terms of influencing other structures as they contain the most amount of kinetic energy. Following from these large scales is the inertial subrange, where the turbulent kinetic energy is transferred to smaller and smaller scales. The eddies in this range are statistically isotropic, meaning that they are inherently easier to model. After the inertial subrange is the dissipation range, where the fluid's viscosity dissipates the remaining energy of the turbulence. The grid size implemented in the simulation will define the amount of the inertial subrange that is resolved by LES and the amount that is modeled by the SGS model. The turbulent kinetic energy spectrum in the current work at a point 10 m upstream of the heliostat at a height of 1.5m and 2.0m (with the HCL being at 1.9m) can be seen on the graph in Fig.7. The sampling location is depicted in Fig.8. The profiles are compared to the Davenport (1961) and Von Karman profiles (Manwell et al., 2009), as well as that obtained by Peterka (1986), of which the velocity and turbulence intensity profiles were used as basis for the current CFD simulations. An indication of the Emes et al. (2018) wind tunnel data is also shown on the graph. The order of magnitude of the current CFD turbulence spectra is comparable to the other profiles, with the CFD suffering from a similar drawback as wind tunnel data in that the lowest frequencies cannot be

capured due to domain size and total simulation time restrictions. The Kolmogorov decay rate (-2/3 in non-dimensional scale) is followed approximately.

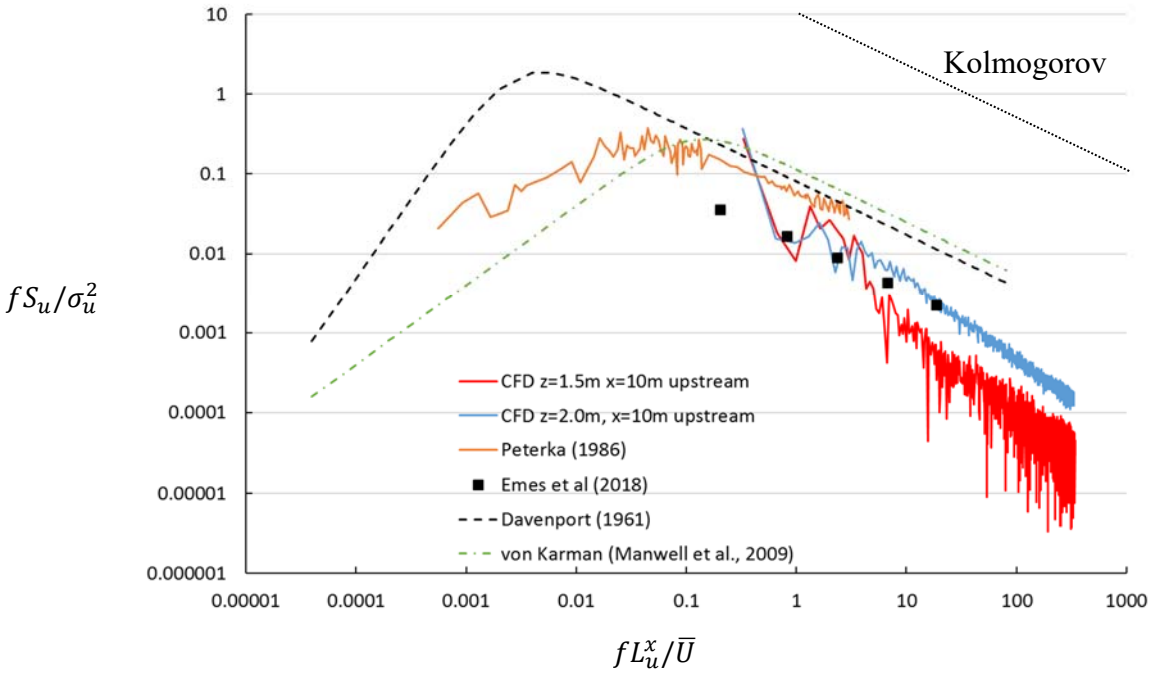

Figure 7. SBES simulation freestream turbulence spectra at 10m upstream point at two heights (1.5 and 2 m) compared to wind tunnel data (Peterka (1986), Emes et al. (2018)) and correlations of Davenport (1961) and Von Karman (Manwell et al., 2009).

The integral length scale which represents the sizes of the largest eddies that correspond to the largest magnitudes of the power spectra (Fig. 7) at a given height in the ABL, need to be matched too. Taylor's hypothesis that eddies do not evolve with time as they are embedded in a frozen turbulence field and are convected downstream at the mean wind speed in the streamwise x-direction is used as in Emes et al. (2018). The streamwise velocity monitored as a function of time at a freestream point situated 10m upstream of the heliostat at the HCL is used to calculate the integral length scale using the autocorrelation method. The autocorrelation function is defined as (Manwell et al., 2009).

$$R(r\delta t) = \frac{1}{\sigma_u^2(N_s - r)} \sum_{i=1}^{N_s - r} u_i u_{i+r} \tag{15}$$

where:
$r = Lag\ number$
$N_s = Number\ of\ samples$
$\sigma_u^2 = Varience\ of\ the\ streamwise\ velocity\ fluctuations$

The integral time scale represents the time taken for the largest eddies to navigate a single point in the ABL. The integral time scale is calculated using equation 22 by the integral of the autocorrelation function (Emes et al., 2016), with τ_0 the lag time of the first zero crossing of the autocorrelation function.

$$T_u^x = \int_0^\infty R(\tau)d\tau \approx \int_0^{\tau_0} R(\tau)d\tau \quad (16)$$

The integral length scale is then calculated by multiplying the integral time scale with the mean velocity at the respective height, z:

$$L_u^x(z) = T_u^x(z)\overline{U}(z) \quad (17)$$

Implementing this method, the integral length scale at a location 10m upstream of the upright (0°) heliostat was determined as a function of height above the ground using monitored x-velocity data for a period of about 6 seconds.

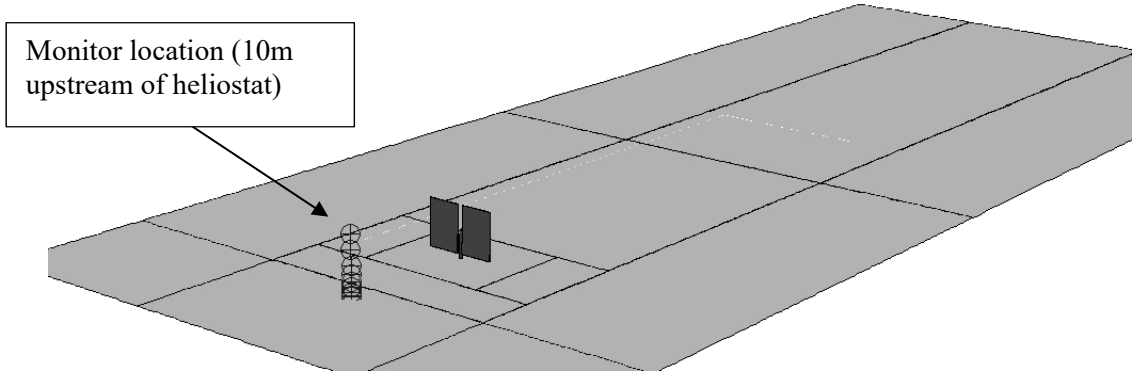

Figure 8. Monitor location for turbulence spectrum, velocity profile and integral length scale calculation

The calculated integral length scale is shown in Fig.9 as a function of height. The profile is compared to that of a low roughness full-scale atmospheric boundary layer in Utah as reported by Emes et al. (2016). For the latter, the first zero crossing of the autocorrelation function was also used. The integral length scales calculated in the current work exhibit a similar trend as the measured full-scale results but are smaller. The presence of the heliostat obviously influences the size of the turbulent structures, but this cannot be quantified without performing an empty domain simulation.

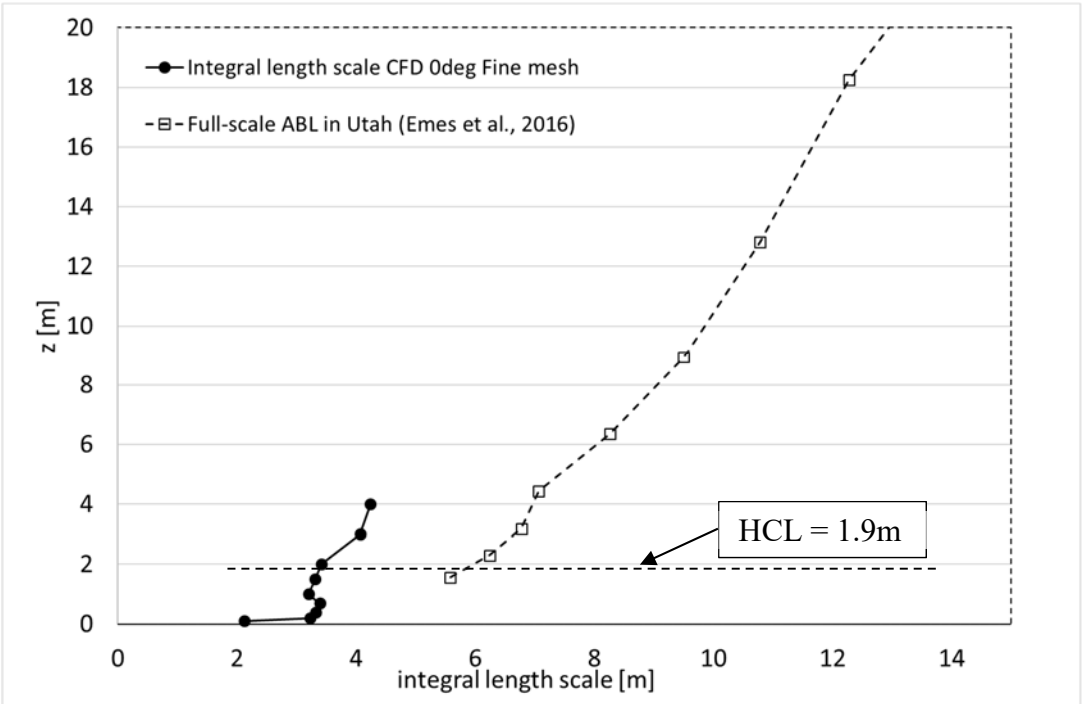

Figure 9. Integral length scale versus height as a location 10m upstream of the heliostat. Current CFD (0 degree fine mesh) compared to a full-scale measurement in Utah (Emes et al., 2016)

4.4 Results

The aim of performing SRS simulations on the heliostat is to obtain transient loadings on the structure as well as peak loadings and to determine the main frequencies present in the vortex shedding in order to design away from potential structural damage and self-excitation. Two separate simulations are conducted at both 0° and 60°, corresponding to the critical drag force and torque-tube moment as discussed previously. The results of the fine mesh 0° and 60° cases are shown in Fig.10. These include the velocity magnitude at a point monitor in the wake of the heliostat at HCL height (Fig.10A and 10C) (x = 14 m, y = 1.9 m) and drag coefficient plots for both cases (Fig.10B and 10D). The lift coefficient (Fig.10E) and the torque-tube moment coefficient (Fig.10F) are displayed for the 60° case.

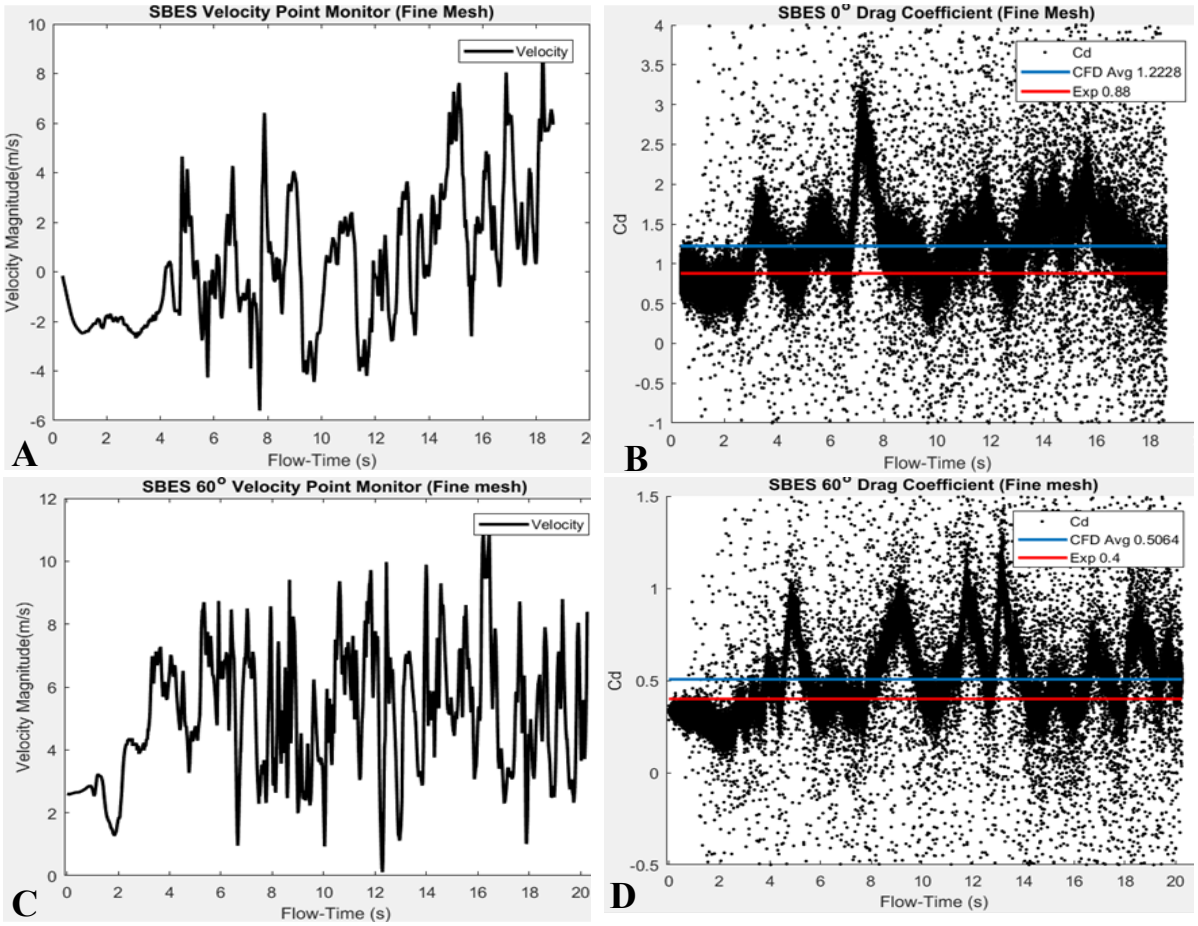

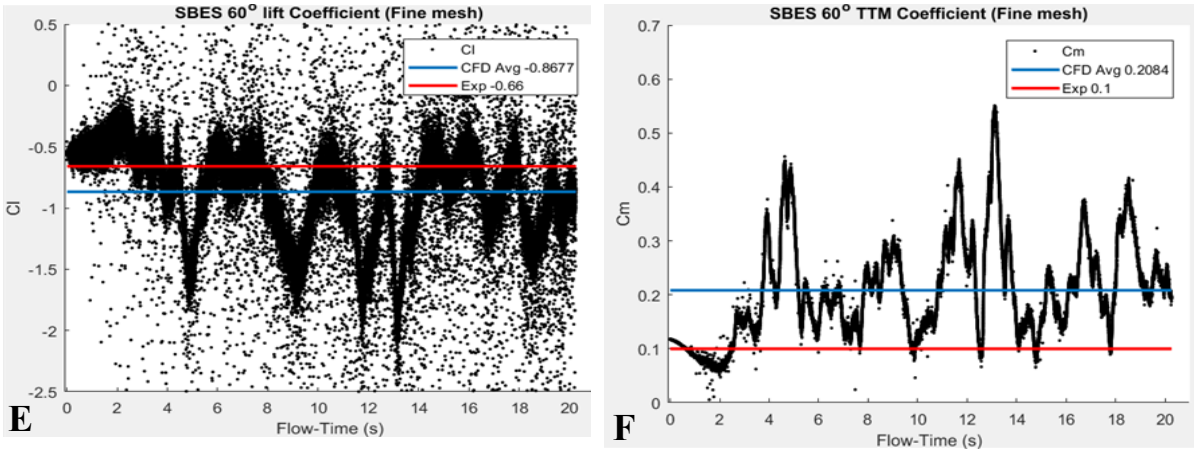

Figure 10. A) Velocity magnitude monitor point in wake for 0° case. B) Drag coefficient of 0° case. C) Velocity magnitude monitor point in wake for 60° case. D) Drag coefficient of 60° case. E) Lift coefficient for 60° case. F) Torque-tube moment for 60° case. The experimental values (red lines) refer to the RWDI wind tunnel results as portrayed in Fig.5 (Huss et al., 2011)

Looking at the velocity monitor point plots, the abundant amount of frequency content present in the flow is evident. This content is only possible with SRS modeling.

Previous research into wind loads on heliostats and other solar collectors and panels has been performed by Ghanadi et al. (2016) and presented by Pfahl et al. (2017). This work on unsteady computational fluid dynamics shows the increase in the peak load related to the increase in the turbulence intensity. At a turbulence intensity of 18% the variation of the amplitude can be equivalent to the mean load, this corresponds to the values measured by Peterka and Derickson (1992) and the findings of the SBES CFD simulations in this study. The 0° case loading case (Fig. 10B) shows the mean drag value of 1.2228 with the peak values around 3 with the 60° case (Fig. 10D) mean drag of 0.5 with the peak values of approx. 1.

The fine mesh drag coefficient results for the 0° case were determined from from 0 to 19 seconds. The first observation from Fig.10 is that the simulations probably need to be run longer for the average values to converge. The computational cost associated with these runs is high and utilized 240 cores at the Center for High Performance Computing in Cape Town, South Africa, requiring several months to generate the results presented here. Nevertheless, some trends in average values can be seen. The mean drag coefficient value for the 0° case for the period is 1.223. The deviation from the experimental mean value (Fig.5) is 28%. The 60° drag coefficient deviation from the experiment is 21%, lift coefficient is 24% and the torque-tube moment coefficient is 51%. The rather large deviation between the SBES and experimental flow results seen in the fine mesh is most likely due to the need for further run time as the flow field is only just developing. Another reason for this nonconformity is due to the uncertainty in the turbulence intensities and mean flow profile prevalent in the experimental tests and the fact that they were performed on a scaled heliostat.

Visible in the drag and lift coefficient plots (Figs.10B, D and E) is the sporadic nature of the points. These spurious outlying points are believed to be caused by the vortex method. They are most likely due to spurious non-physical pressure fluctuations believed to be caused by the method's random switching of vortex rotation and the underlying possible violation of mass local mass conservation, especially given the current incompressible flow assumption of the simulation. These spikes involve the whole flow domain and are of a very short duration (one or two time steps). Because of the latter, they do not affect the force field or force averages significantly. A recent update in ANSYS Fluent (v19.2) did start to resolve this phenomenon by providing a mass conservation option for the Vortex method.

Shown in Fig.11 is the fine mesh drag coefficient signal compared with the coarse mesh signal for the 0° case. The mean of both signals is shown along with the Root Mean Square (RMS) and Standard Deviation (SD) of the signals. The fine mesh is shown to capture more peaks and detail than the coarse mesh. This is evident simply by looking at the signal but can be confirmed by the higher RMS value. The RMS value gives the square root of the mean data squared thus provides an indication of the mean taking into account and giving emphasis to the peak values. The SD value also shows that the fluctuation of the fine mesh data is far greater than the coarse mesh result, evidence of the peak forces and turbulence being better resolved and captured. There is a greater amount of frequency content visible in the fine mesh signal, again indicative of the superior capability of the fine mesh to resolve a greater amount of turbulent content in the flow, compared to the coarse mesh. The increase in the mean drag coefficient can be attributed to the increase in the size of the peaks of the force.

In Fig.12 similar results for the torque-tube moment coefficient signals can be seen. The fine mesh result has a mean moment value of 0.2084. While this value deviates from the experimental value (Fig.5) by some margin, it is comparable to the results of Peterka (1989). In the results from Peterka (1989), the mean torque-tube moment coefficient is given as 0.27 while the peak value is given as 0.6. This provides some validity to the SBES results as the Peterka heliostat is comparable in size to the heliostat used in this study.

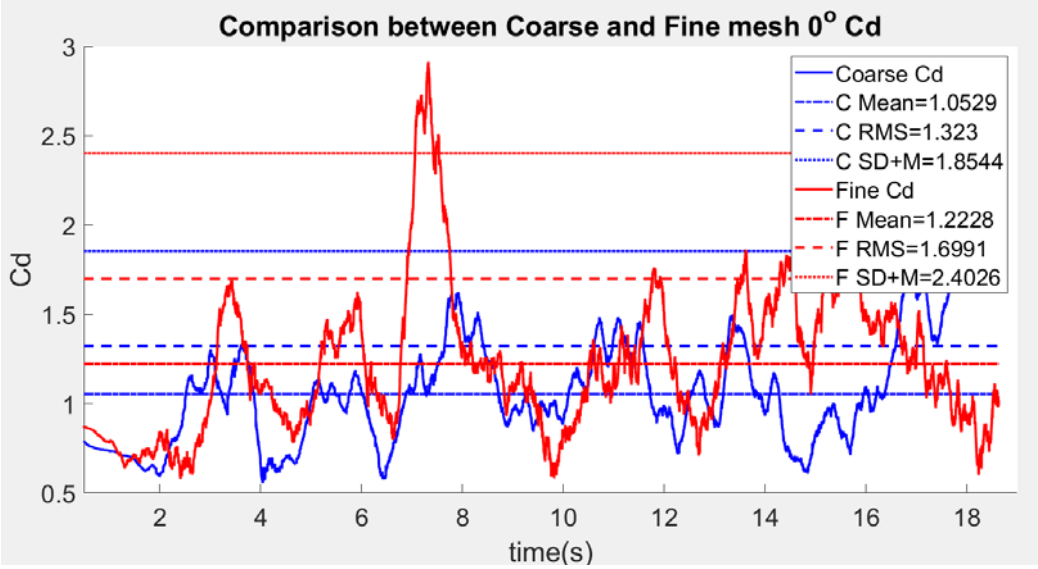

Figure 11. SBES simulation, comparison between fine and coarse mesh 0° drag coefficient, Cd.

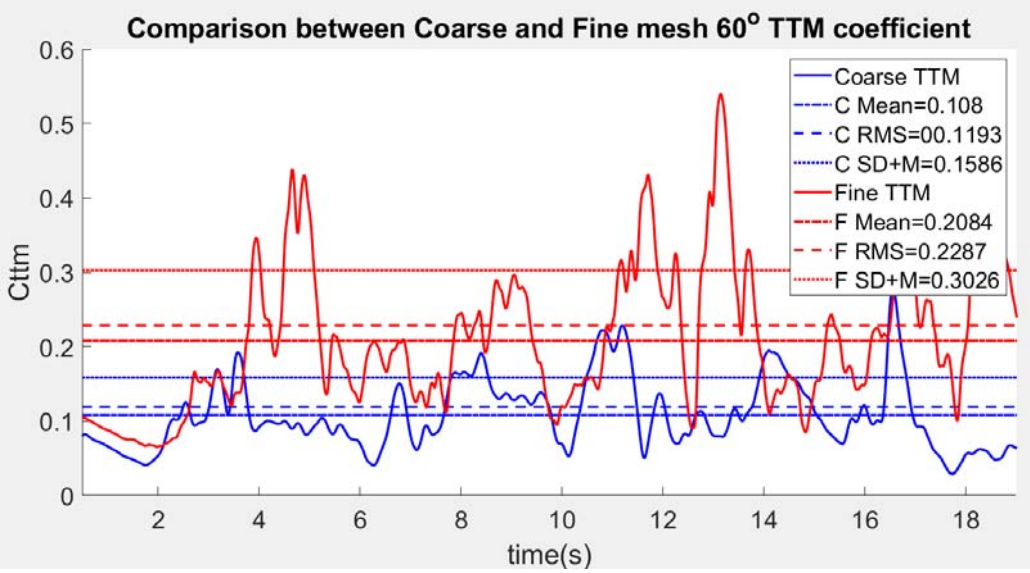

Figure 12. SBES simulation, comparison between fine and coarse mesh 60° torque-tube moment, Cttm.

Modeling the ABL with SBES also leads to horizontal homogeneity problems, i.e., a lack in the ability to maintain the inlet profiles of mean velocity and turbulence intensity up to the heliostat location. This can be seen with the x-direction turbulence intensity profile prescribed at the inlet as well as at 5 m upwind from the heliostat, as displayed in Fig.13A and compared to the ABL profile of Peterka (1986). The intensity specified at the inlet HCL is 20%. By the time the profile reaches the heliostat, the instantaneous turbulence intensity is close to this value at the HCL. This is one possible reason for the disagreement between the experimental torque-tube moment coefficient value and the SBES value. According to Peterka (1989), a difference in the turbulence intensity can lead to a large difference in the aerodynamic coefficient values. A difference of 18% in the turbulence intensity of the torque-tube moment coefficient can lead to a difference of 81% in that coefficient (Peterka, 1989). Likewise, a difference in turbulence intensity of 17% can lead to a 42% difference in the drag coefficient.

Noteworthy is the fact that Huss et al. (2011) states that the turbulence intensity of 20% is achieved in the wind tunnel at the inlet of the tunnel at the scale HCL. As stated earlier, whether this intensity is achieved downstream at the heliostat, or whether the full-scale result is comparable, is unknown. The instantaneous SBES inlet turbulence intensity profile deviates from that of Peterka (1986) due to the vortex method's influence and can be seen to further change as it is transported downstream due to the interaction of turbulent structures and the influence of the heliostat's blockage downstream. The shape of the instantaneous profile 5m upstream of the heliostat still shows some resemblance to the inlet profile. In other SRS simulations of an empty wind tunnel (Poulain et al., 2016)), the hybrid RANS approach was able to achieve a level of horizontal homogeneity. Here, the aim is to replace the upstream development section of the domain (or wind tunnel) with a representative profile. The heliostat and interaction between turbulent structures clearly influences both the turbulence profiles as well as the mean veloctity profile. The latter is shown in Fig.13B at the inlet and a point 10m upstream (about 3 chord lengths) of the heliostat in the upright orientation. The time-averaged inlet profile matches the specified logarithmic profile fairly accurately but the profile closer to the heliostat deviates from this inlet profile as it starts to accelerate due to the presence of a recirculation zone before the heliostat.

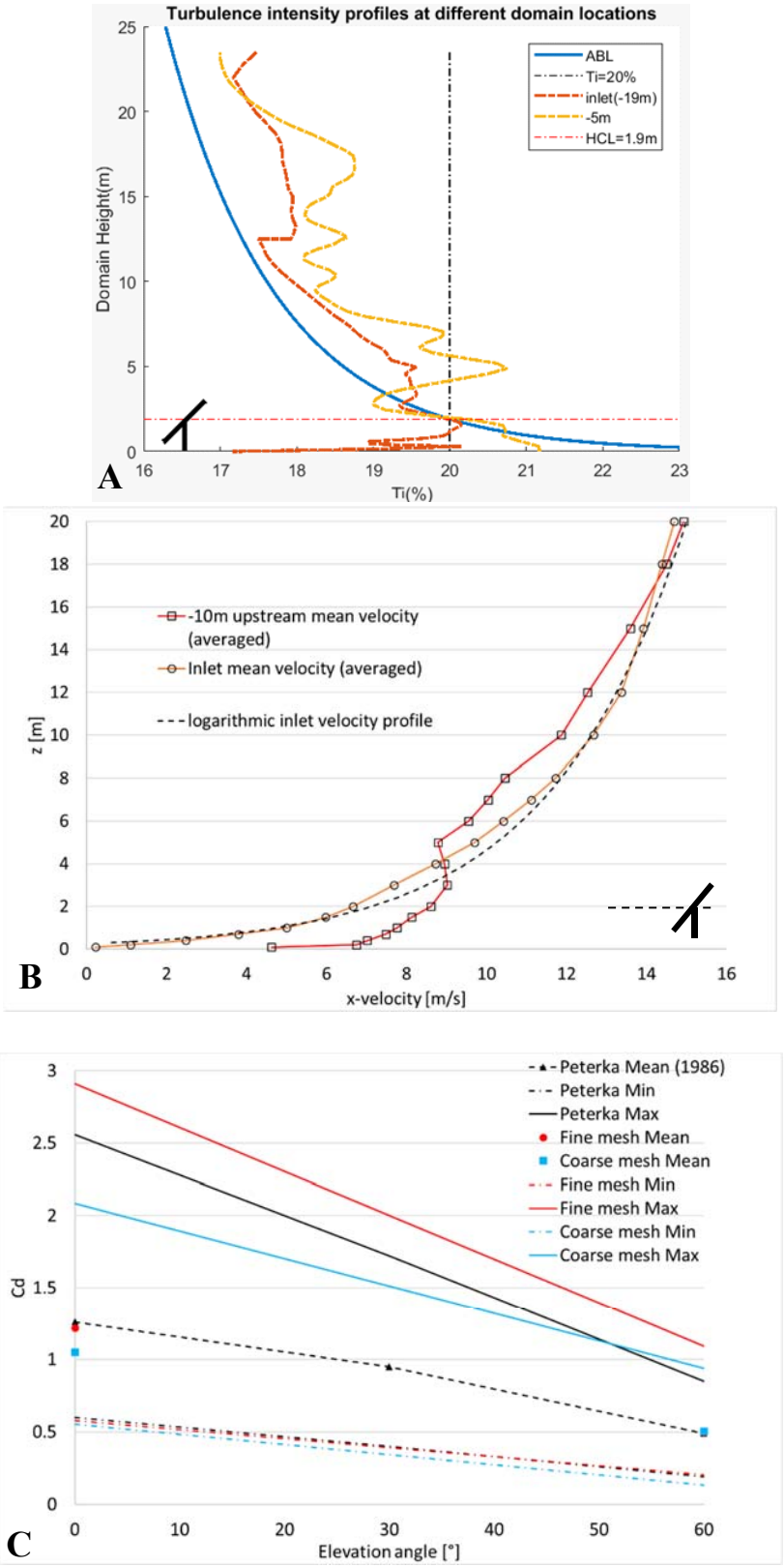

Figure 13. A) Instantaneous turbulence intensity profiles at different domain locations. B) Mean velocity profiles at inlet and 10m upstream of the heliostat. C) SBES drag coefficient results as function of elevation angle compared to (Peterka, 1986).

In Fig.13C, the 0° and 60° drag coefficients for both the coarse and fine mesh are compared to the 0°, 30° and 60° results of Peterka (1986). The mean value of the experimental results is shown along

with the maximum and minimum drag values. The SBES simulation points are shown with the corresponding minimum and maximum values for the coarse and fine meshes for the duration simulated. This is plotted as an additional means of validating the SBES results. The fine mesh mean SBES drag lies almost exactly on the experimental mean. The coarse SBES results are also fairly close to the experimental mean. Interestingly though and as shown previously, the fine mesh variation is considerably greater than that of the coarse mesh for the 0° case and is comparable to the upper peak value of Peterka (1986). The data for the 60° case are almost identical between the fine mesh, coarse mesh and experimental values.

Turning next to the frequency content of the flow, power spectral density (PSD) plots are depicted in Fig.14. As can be seen in Fig.14A, there is low frequency content in the freestream flow that may influence the response of the heliostat regardless of vortex shedding. This low frequency content is representative of the larger energy containing turbulent structures in the flow. Comparing the PSDs for the upstream velocity (Fig.14A) and the wake velocity point monitors (Fig.14B and 14C), it can be seen that some of the very low frequency content still exists in the wake region as would be expected. E.g., the 0.444 Hz spike in Fig.14A is shifted to 0.499 Hz in the wake velocity point monitor (Fig.14B). This 0.499 Hz is the vortex shedding frequency from the heliostat at 0°. Looking at the PSD of the velocity magnitude monitor point in the wake of the heliostat for 0°, Fig.14B, there exists a frequency of 1.1 Hz, double the vortex shedding frequency, due to the monitor point catching the front and back of a single vortex. The coarse mesh used in the wake region of the heliostat flow is unable to resolve the accurate vortex shedding behavior and subsequent frequencies. This can be seen in Fig.14B, as the vortex shedding frequency spike is incorrect for the coarse mesh and the secondary spike, representing the double vortex-shedding frequency, is hardly present in the PSD. Previous experimental research conducted by Mammar et al. (2018) on heliostat wind loads reported a Strouhal number of approximately 0.14 for a heliostat at 85° orientation (equivalent to 5° in this study, so close to being upright). This is a 7.8% difference compared to the Strouhal number of 0.152 found for the 0° case using SBES.

For the 60° case the results are more interesting. With the freestream frequency content of the upwind flow containing such low frequencies it makes it difficult to distinguish which frequency components are due to vortex shedding and which are as a result of the general (upstream) flow field. Looking at the velocity point monitor, Fig. 14C, spikes at 0.65 Hz, 1.11 Hz and about 1.3 Hz can be seen. Taking the spike with the highest amplitude as a candidate for the main vortex shedding frequency, 1.1 Hz can be considered to be the vortex-shedding frequency for the 60° SBES case.

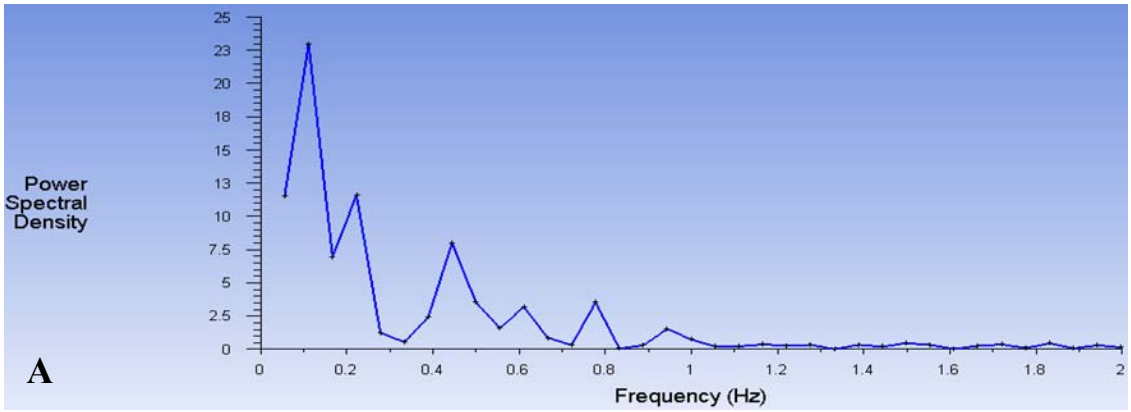

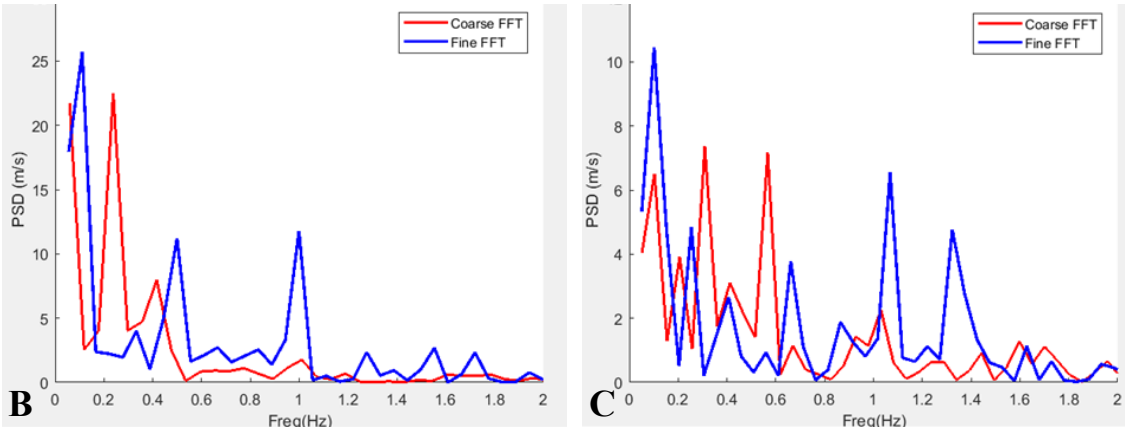

Figure 14. A) PSD of the SBES upwind freestream velocity magnitude monitor point. B) Comparison between Coarse and Fine mesh 0° wake velocity magnitude point monitor PSD. C) Comparison between the Coarse and Fine mesh 60° wake velocity magnitude monitor point PSD.

Finally, Fig.15 depicts the evolution of turbulent structures for the upright (0°) case in the form of Q-criterion iso-surfaces. It is evident that turbulent structures from the upstream flow interacts with those generated by the heliostat. In addition, there is a 'snaking' pattern evident in the wake when one compares the time series snapshots.

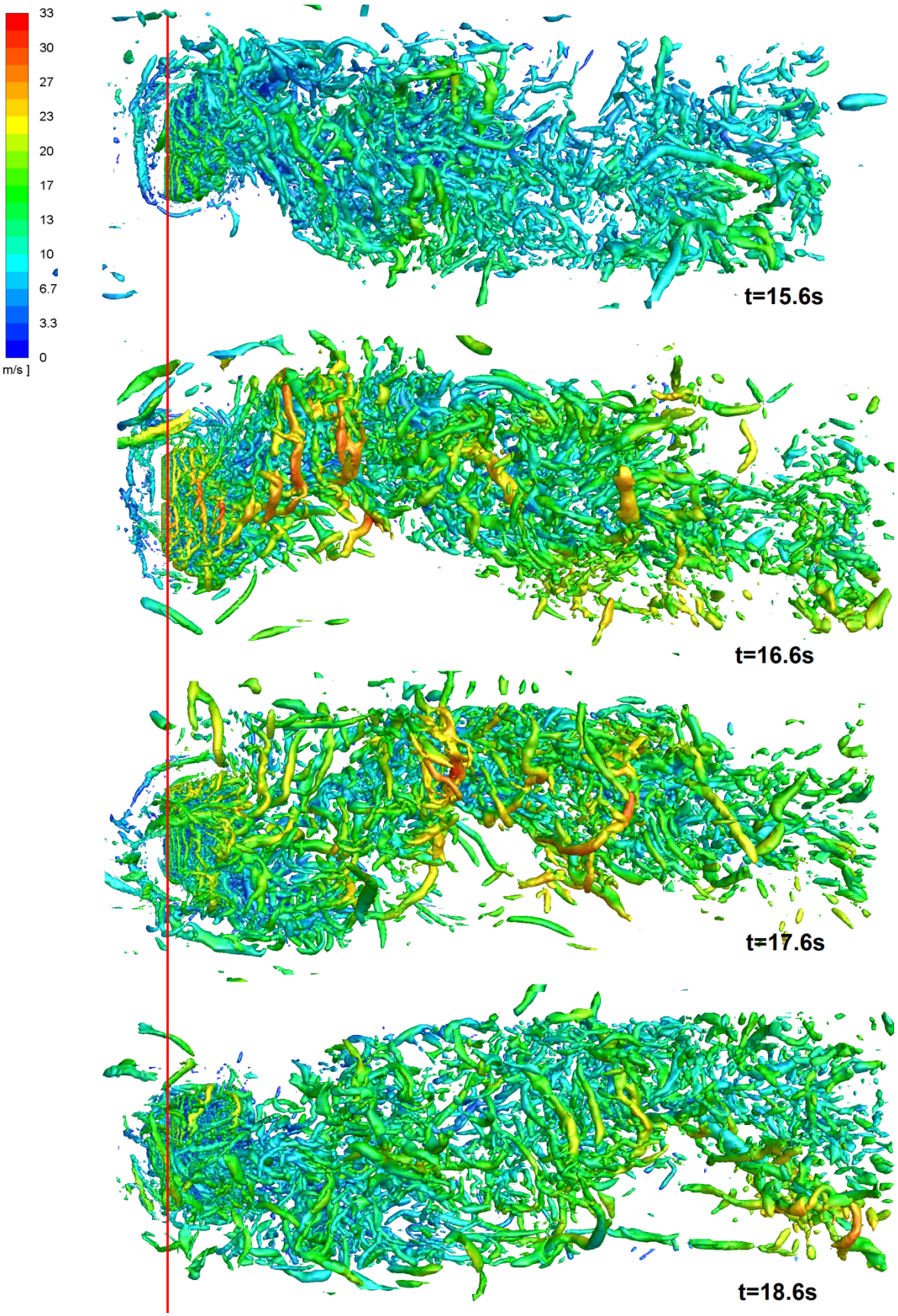

Figure 15. Time series of Q-criterion iso-surfaces (Q=100 s^{-2}) colored by velocity magnitude between 15.6 and 18.6 seconds. The red line indicates the heliostat location in this top view. 0° case, SBES.

5. ONE-WAY FLUID-STRUCTURE INTERACTION

The SBES SRS CFD results from the previous section were used to perform the one-way fluid structure interaction. During the CFD simulation, the static pressure on the front and back mirror faces as well as the torque-tube and pylon surfaces were extracted. These extracted data were written to comma-delimited ASCII files. The data contained in each file consisted of each fluid mesh node number, the nodes' position in Cartesian coordinates and the relevant static pressure value at each node. The CFD simulation had a time-step of 0.0003 seconds. The pressure files were extracted every 10 time-steps or every 0.003 seconds. In total for the 0° heliostat configuration, at the end of the simulation reported on in the previous section, 990 pressure files were extracted resulting in 2.97 seconds of flow time. For the 60° configuration, 796 files, resulting in 2.388 seconds, were extracted. These pressure files were imported into an External data component in the ANSYS Workbench environment. This process required around 6 hours to complete. The files were processed in batch inside this External data component before being linked to a Transient Structural component using ANSYS Mechanical. A sample imported pressure distribution is shown in Fig.16 for the front face of the 0° heliostat orientation.

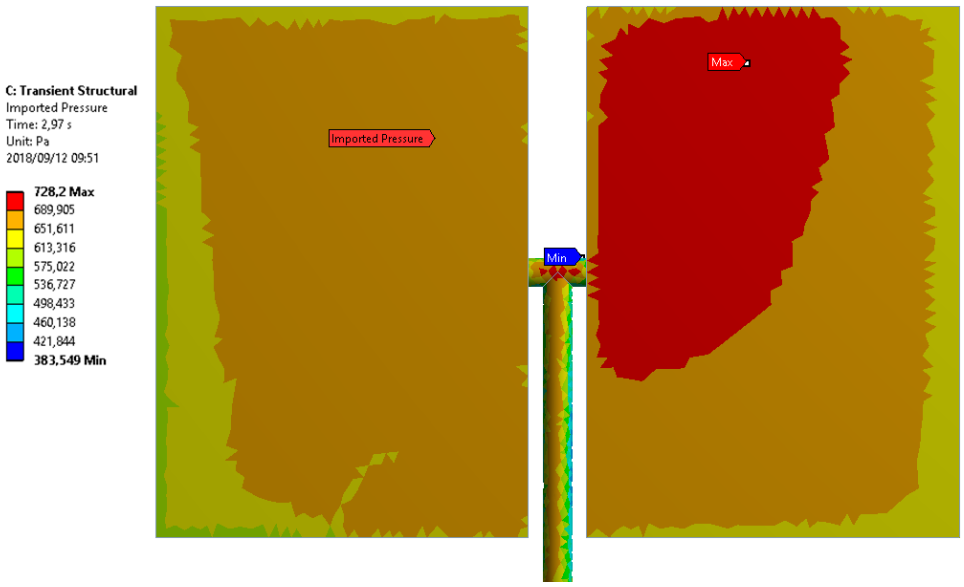

Figure 16. Sample imported pressure distribution on front face of heliostat. 0° case.

The heliostatsolid model was meshed with 3D tetrahedral elements with a maximum size of 5 cm and contains approximately 30 000 elements. The model was assigned the properties of Structural Steel, as listed in Table 2.The base of the pylon is assigned as a fixed support boundary. The analysis settings used in the one-way FSI simulation for the 0° configuration are as follows, the step end time is set at 2.97 s with auto time stepping set to off and the time step size prescribed as 0.003 seconds. The only change to the analysis settings for the 60° configuration is the step end time is set as 2.388 seconds. The CFD simulation time used to extract the pressure files is from 15 seconds, thus the flow field can be assumed to be developed, as this equates to 1.5 flow-through times for the computational domain. The wall thickness of the torque-tube and pylon is 6 mm.

Young's Modulus	$2x10^{11}$ Pa
Poisson's Ratio	0.3
Density	7 850 kg/m^3

Table 2: Structural steel material properties of heliostat.

The mode numbers and corresponding frequencies for both cases are given in Table 3. The modal frequencies and shapes are critical to this structural investigation as the deformation of the heliostat due to the flow field may excite a specific modal shape even if that mode is not at the vortex-shedding frequency. The heliostat vortex shedding frequency needs to be designed away from modal excitation of the structure to ensure resonance is not achieved, leading to premature structural damage. The first three modes for each configuration are briefly desrcibed as, **0°,** 1st mode is a rocking motion from side to side about the pylon base. The 2nd mode is the two extreme edges of each mirror flexing back and forth. The 3rd mode is the top edge of the mirror flexing back and forth. For the **60°** configuration, the 1st mode is the flexing of the side edges back and forth. The 2nd mode is characterised by the rocking of the heliostat side to side while the 3rd mode is rocking back and forth.

Mode	Frequency (Hz) (0°)	Frequency (Hz) (60°)
1	1.9799	1.9272
2	2.2244	2.1123
3	2.699	2.636
4	5.485	6.0066
5	6.0105	6.4593
6	6.135	6.517
7	7.3064	7.5317
8	12.672	10.721
9	17.68	18.325
10	18.474	18.781

Table3: Modes of 0° and 60° cases.

The Transient Structural one-way FSI results for the 0° heliostat case are presented next. The response of the heliostat structure to the transient pressure loads derived from the SBES scale-resolving CFD simulation is investigated. Particular importance is placed on the vibrational response of the structure in line with the vortex-shedding frequencies. Although the deformation of a heliostat is critical to the efficiency of an operating plant, it is not scrutinized in this section. The same can be said for the stress induced in the structure due to the pressure, provided the yield stress of the material is not surpassed, no further investigation is performed. For both the 0° and 60° cases, four important structural results were looked at. These included the directional deformation of critical points on the structure, the total deformation of the structure, the equivalent stress of the structure and the reaction force of the fixed support. These were then analyzed and a PSD of the resultant graphs produced in order to draw comparisons to the CFD results and conclusions from the heliostat responses.

For the 0° case, the graph of the response signal of the top right mirror vertex is shown in Fig.17A, while for the 60° case, the response signal for the top right vertex in both the x-axis and z-axis, are depicted in Fig.17B, C, respectively.The results from the displacement of the top right mirror vertex show that for the 0° case the response signal has a very smooth sinusoidal behavior. The maximum displacement seen by the vertex is 6.2 mm. It appears as though there is a single driving frequency in the signal. This is confirmed via the PSD of the Fig.17A signal which shows a large single spike at 2.69 Hz (Fig.17D). It is evident that this frequency is well outside the vortex-shedding frequency simulated in the previous section of 0.499 Hz. Looking at the table of mode shapes for the 0° case (Table 3), the 3rd mode has a frequency of 2.699 Hz. It appears that the heliostat, under the agitation of the SRS pressure field, is being excited at this modal frequency. This is due to the deformation of the

structure being in line with this particular mode shape. The 60° case x-axis vertex displacement signal shown in Fig.17B is not as smooth as the 0° case. This reveals that there is underlying content present in the signal that needs to be examined. The PSD of this signal (not shown) produced a frequency 2.1 Hz. As with the 0° case, this frequency is far from the vortex shedding frequency obtained with the SRS CFD simulations of 1.11 Hz or 1.3 Hz (Fig.14C). Further investigating how the vertex displaces in the z-axis direction, the signal in Fig.17C is obtained. The PSD of this signal (not shown) confirmed two dominating frequencies of 2.1 Hz and 6.31 Hz. These frequencies once again are due to the heliostat structure being deformed to the shapes of and thus being excited at the 3rd mode and a combination of the 4th, 5th and 6th modes (see Table 3).

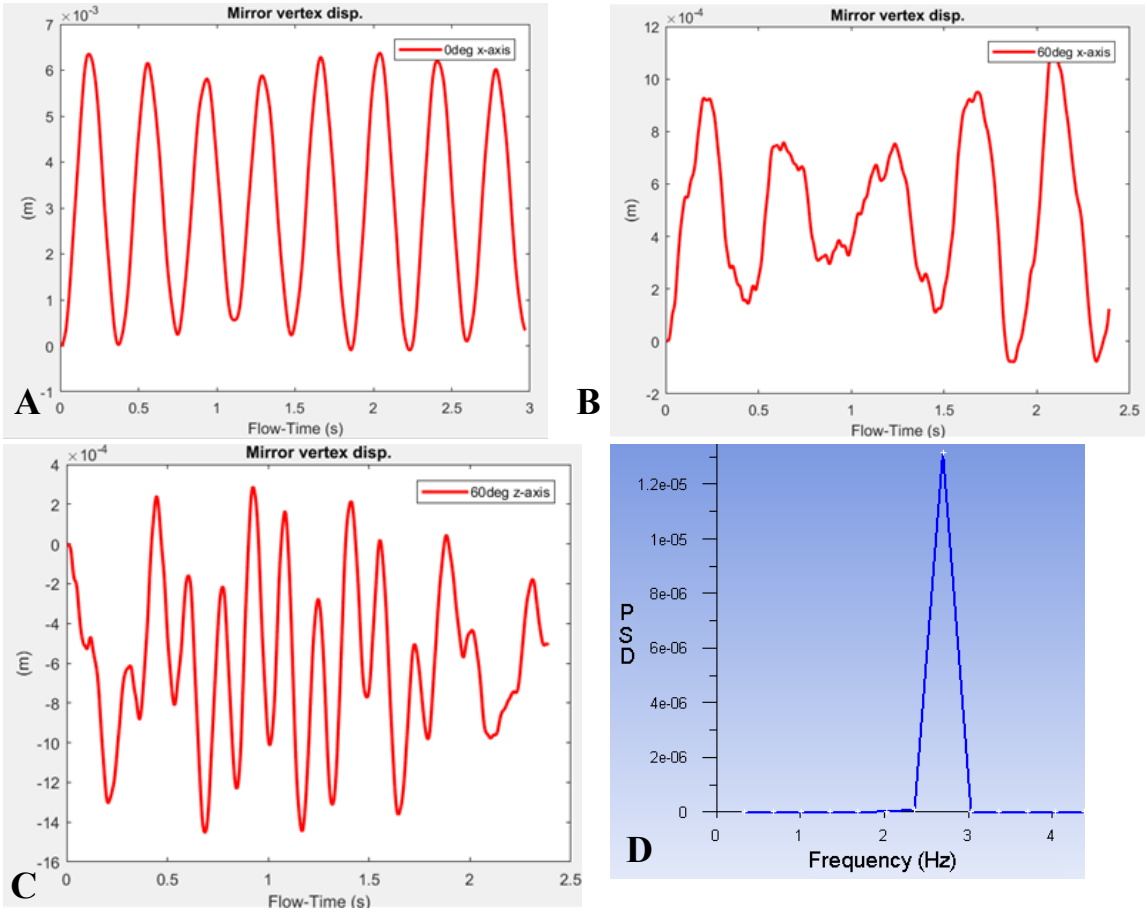

Figure 17. A) Top right vertex displacement (x-axis) for 0° case. B) Top right vertex displacement (x-axis) for 60° case. C) Top right vertex displacement (z-axis) for 60° case. D) PSD of signal in Fig.17A.

The previous results were for a specific vertex located on the heliostat mirror. Now the total deformation of the entire heliostat structure and maximum Von Mises stress is investigated for both cases. The total deformation of the heliostat for the 0° case is shown in Fig.18A, followed by the deformation of the 60° case, in Fig.18B.

The deformation of the heliostat for this 0° case is dominated by the entire heliostat deflecting backwards in the direction of the fluid flow. This is the logical deflection of any structure being attacked with the force due to the fluid flow being normal to the mirror faces. The total deformation signal of the 0° case shows a similarity to the vertex displacement signal in the almost smooth sinusoidal nature of the signal. The PSD (not shown) confirmed a dominating frequency component of 2.69 Hz, the exact same frequency found in the vertex displacement signal. Looking at the maximum deformation of the

60° structure in Fig.18B, one can see that the main shape of the deformation has shifted from the 0° case of back and forth to the 60° case of side to side. This was confirmed when looking at the mode shapes of these excited frequencies. The total deformation signal of the 60° case once again contains a considerably greater amount of frequency content when compared to the 0° case. A PSD confirmed that the strongest frequency present is a 2.1 Hz peak followed by a second 5.89 Hz peak and a smaller 6.73 Hz peak. This means that the behavior of the structure is dominated by the 3rd mode which could be assumed as a side-to-side mode and a combination of the other modes mentioned earlier.

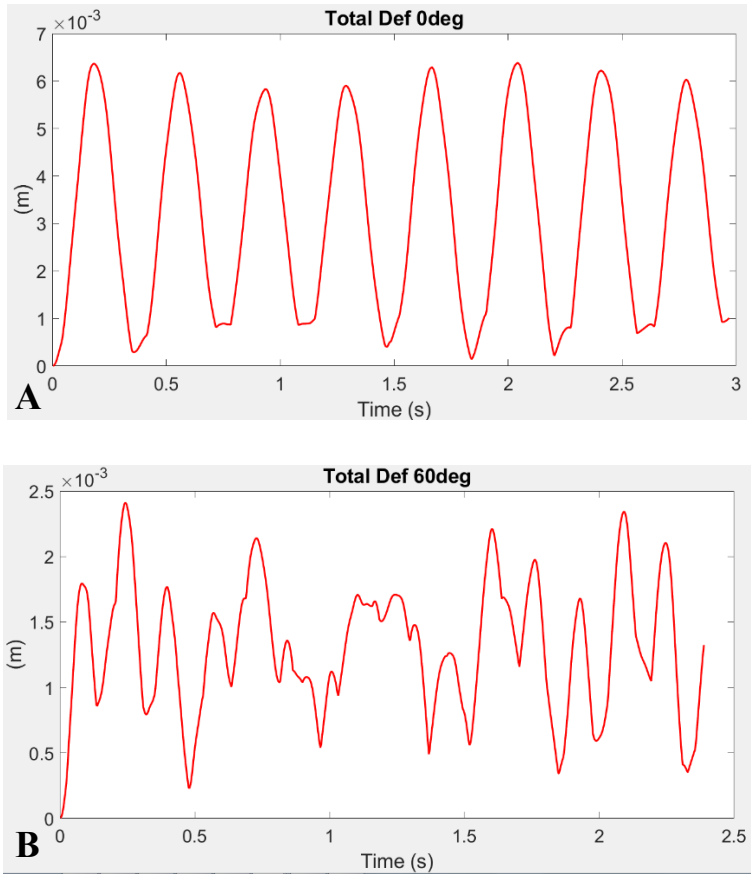

Figure 18. A) Total deformation signal for 0° case. B) Total deformation signal for the 60° case

The maximum stress in the 0° structure displays the time history in Fig.19A following the sinusoidal behavior and frequency of the deformation. Shown in the contour plot of the stress for the 0° heliostat (Fig.19B), the highest induced stress in the structure over the loading period is 39 MPa. This is well below the yield strength of structural steel as expected as the mean wind velocity considered is only 10 m/s. The aim of investigating the stress profile for the heliostat is to see which areas of the structure experience the greatest stress and examine the resultant PSD of the stress signal. The peak stress is seen to be located near the base of the heliostat on the back face of the pylon. This compressive stress has an opposed tensile stress as seen on the front face of the pylon. This stress profile is expected due to the large bending moment seen by the pylon as it opposes the oncoming wind pressure. Very little stress is induced in the mirrors and backing structure with a small stress seen in the torque-tube near the intersection with the pylon. The critical member in this case would be the pylon.

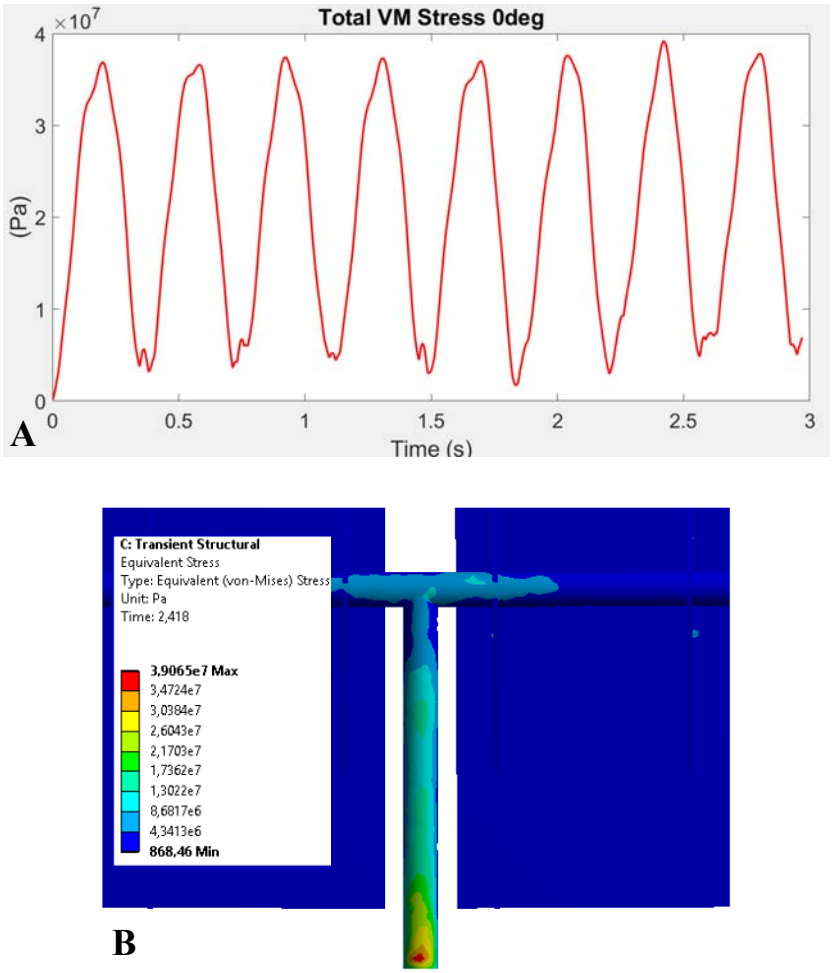

Figure 19. A) Maximum von Mises stress signal for the 0° case. B) Maximum von Mises stress contour for the 0° case.

Looking at the stress contours for the 60° case (Fig.20B), the maximum induced stress in the heliostat has decreased by about half to 16 MPa. This is expected as the frontal mirror area has decreased by approximately half. Interestingly the location of the maximum stress is no longer seen at the base of the pylon but is now located at the T-joint between the torque-tube and the pylon (an actual heliostat has a completley different joint between the torque-tube and pylon). This joint is now the critical member of the structure at 60°. This may be due to the different motion of the heliostat at this angle, compared to 0°. Here there is side-to-side motion mixed with the mirrors flexing backward. This is compounded by the peak torque-tube moment experienced at 60°. Looking at the stress signal (Fig.20A), it is evident that there are multiple different frequencies present. The PSD (not shown) confirms a considerably smaller 2.1 Hz component compared to the previous 60° signals while the major frequency present is 5.89 Hz and 6.7 Hz. As stated earlier there are three modes in the 6 Hz range (Table 3). The result of the 60° stress signal frequencies is due to the heliostat deflecting with these mode shapes simultaneously.

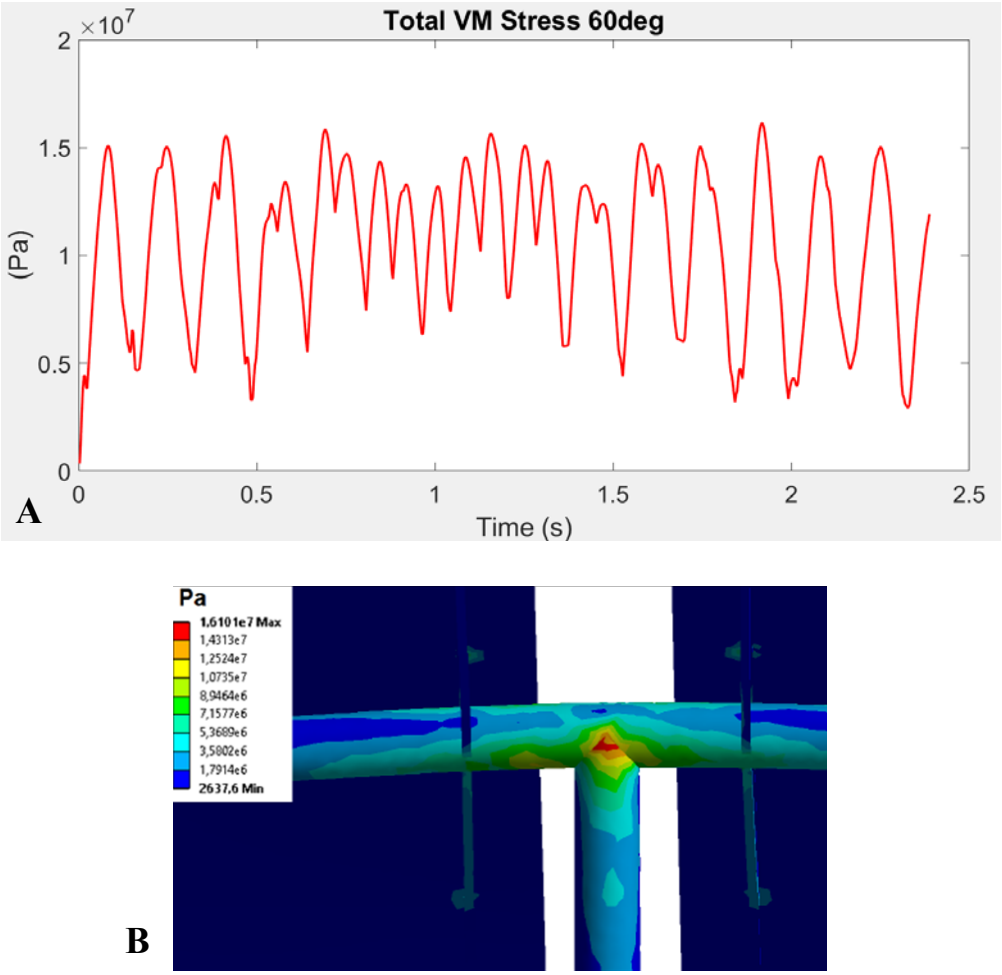

Figure 20. A) Maximum von Mises stress signal for the 60° case. B) Maximum von Mises stress contour for the 60° case.

Even though the heliostat produces a defined vortex shedding frequency for its given configuration, the response of the structure appears to be more complex and involved than simply oscillating at this shedding frequency. The SRS CFD simulations produce a large amount of frequency content that can excite the heliostat. More importantly it seems as though the specific mode shapes for both the 0° and 60° cases happen to exist at the same deformation shapes one would expect of the heliostat in the fluid flow. This is no coincidence as the mode shapes illustrate how the structure would want to naturally deform. The vortex shedding of the 0° case calculated from the SBES simulations is 0.499 Hz. The structural response of the heliostat furnished with the pressure field derived from the SBES simulation is dominated by a 2.69 Hz frequency. This is exactly the frequency of the third mode of the heliostat at 0°.

6. CONCLUSION AND FUTURE WORK

The paper considered the simulation of the one-way fluid-structure interaction of a medium-sized heliostat at two wind orientations. As realistic input to the transient structural simulation, use was made of scale-resolving computational fluid dynamics in the form of the SBES method, a hybrid RANS-LES approach. The following conclusions can be drawn from the results presented:

- The Reynolds-Averaged Navier-Stokes approach can only be used to predict mean wind loads on heliostats. For this, careful implementation of the atmospheric boundary layer (ABL) is

required, both in terms of the mean wind velocity profile as well as the turbulence intensity profile.

- As shown for the orientations considered, Scale-Resolving Simulation in the form of the hybrid RANS-LES SBES model is capable of resolving peak loads and turbulence flow fields that are in line with previous experimental results from the literature. Here, both the integral scale cascade and sample integral length scales in the upstream flow were captured to a reasonable extent. There should however be adequate experimental results of both mean and fluctuating quantities available for comparison when judging the performance.
- The SBES flow results with a rigid heliostat showed evidence of vortex shedding with other frequencies also presented in both the velocity monitor points and calculated force and moment coefficients.
- The response of a medium-sized heliostat after solving for one-way fluid-structure interaction is however not necessarily defined by the vortex shedding. In the orientations evaluated in the current study, the response was primarily dictated by the mode shapes and modal frequencies of the heliostat structure. The loading used was the transient pressure distributions on the heliostat structure obtained from the SBES simulations, thereby providing the transient energy necessary to initiate the oscillatory behavior of the heliostat. It would not be sufficient to merely compare the main vortex shedding frequency computed from an SRS simulation to the modal frequencies. As seen in the study, the heliostat structure is excited at the modal frequencies even though the vortex shedding frequencies are well below the modal frequencies. It can also be concluded from this that the heliostat, at least subject to this flow, is not under threat from self-excitation. Without the use of FSI this information would not be possible.
- The behaviour of the heliostat for the 0° configuration is relatively simple, with a back and forth movement. The movement at the 60° orientation is highly complex and could not possibly be predicted without the use of FSI. The main conclusion is that the heliostat's response to the transient loading is not to react at the vortex shedding frequencies but rather to deform at one or more modal frequencies.

Future work can include:

- More heliostat orientations need to be implemented and simulated for both the azimuth and elevation angles of the heliostat. This is necessary to conclude the accuracy of the 3D SRS vortex shedding predictions.
- The result of this oscillatory behaviour will eventually be increased fatigue and possible damage to the structure if the oscillation amplitudes are large enough.Both the SBES and the FSI simulations should therefore be to investigate the possibility of resonance and early fatigue.
- The SBES simulations needs to be run for a longer period to ensure the flow is further developed so that the averaged aerodynamic forces are accurate and the statistics of the flow are precise.
- The one-way FSI utilising the SRS pressure results should be simulated for a longer period to investigate whether the behaviour established for the approximately three-second period is correct. Structural fatigue should also be further investigated with the oscillatory behavior of the heliostat.
- Two-way FSI utilising SRS CFD is now possible with system coupling on the Centre for High Performance Computing (CHPC) cluster. This needs to be researched and compared to the 1-way FSI.

- Solar traces of the deformed heliostat geometry could be conducted to investigate the amount of radiation that could be lost due to the deflections and oscillations owing to turbulence and vortex shedding.

ACKNOWLEDGEMENTS

The authors would like to acknowledge the support of theUniversity of Pretoria and the South African National Research Foundation (DST-NRF Solar Spoke).In addition, the use of the Centre for High Performance Computing (CHPC) in Cape Town, South Africa, is acknowledged.

REFERENCES

ANSYS, 2018. ANSYS Fluent Theory Guide v19.1, ANSYS Inc., Canonsburg PA, USA.

Bearman, P., 1971, An investigation of the forces on flat plates normal to a turbulent flow, *Journal of Fluid Mechanics 46*, pp.177-198.

Bearman, P.W., 1984, Vortex shedding from oscillating bluff bodies, *Annual Review of Fluid Mechanics 16*, pp.195-222.

Blocken, B., Stathopoulos, T., Carmeliet, J., 2007. CFD simulation of the atmospheric boundary layer: wall function problems. *Atmospheric Environment 41(2),* pp. 238-252.

Bungartz, H. and Schafer, M., 2006. *Fluid-Structure Interaction: Modelling, Simulation, Optimisation*. Berlin: Springer.

Cebeci, T., Bradshaw, P., 1977. *Momentum transfer in boundary layers,* New York: McGraw-Hill Book Co.

Chen, J. and Chiou, C.-C., 1998, Experimental Investigation of a Parallel Vortex-Plate Interaction, *Journal of Fluids and Structures 12*, pp.295-314.

Cook, N.J., 1985, The designer's guide to wind loading of building structures, Part 1: Background, damage survey, wind data and structural classification, In: Building Research Establishment, Garston, UK.

Cruz, E., Watkins, S., Loxton, B. and Watmuff, J., 2008, A flat plate rectangular wing subjected to grid-generated turbulence, in: 26th AIAA Applied Aerodynamics Conference, pp. 6247.

Davenport, A.G., 1961, The spectrum of horizontal gustiness near the ground in high winds, *Q J R Meteorol Soc* 87 pp194–211.

Deaves, D.M. and Harris, R.I., 1978, A mathematical model of the structure of strong winds, In: Report 76, Construction Industry Research and Information Association, London, UK.

Dyrbye, C. and Hansen, S.O., 1996, *Wind loads on structures*, John Wiley & Sons, Chichester, UK.

Emes, M.J., Arjomandi, M., Kelso, R.M., Ghanadi, F., 2016. Integral Length Scales in a Low-Roughness Atmospheric Boundary Layer. *18th Australasian Wind Engineering Society Workshop.* McLaren Vale, South Australia, pp.1-4.

Emes, M.J., Arjomandi, M., Ganadi, F., Kelso, R.M., 2017. Effect of turbulence characteristics in the atmospheric surface layer on thepeak wind loads on heliostats in stow position, *Solar Energy* 157 pp. 284–297.

Emes, M.J., Ghanadi, F., Arjomandi, M., Kelso, R.M., 2018. Investigation of peak wind loads on tandem heliostats in stow position. *Renewable Energy 121,* pp. 548-558.

Gerasimov, G., 2016. *Quick Guide to Setting Up LES-type Simulations V.1.4,* Sweden: ANSYS Inc.

Ghanadi, F., Yu, J., Emes, M., Arjomandi, M., Kelso, R., 2016. Numerical Investigation of Wind Loads on an Operating Heliostat, *SolarPACES2016*, Abu Dhabi, United Arab Emirates.

Gong, B., Li, Z., Wang, Z., Wang, Y., 2012. Wind-Induced Dynamic Response of Heliostat, *Renewable Energy* 38, pp. 206-213.

Gong, B., Wang, Z., Li, Z., Zang, C., Wu, Z., 2013. Fluctuating Wind Pressure Characteristics of Heliostats, *Renewable Energy* 50, pp. 307-316.

Griffith, D.T., Moya, A.C., Ho, C.K. and Hunter, P.S., 2015. Structural Dynamics Testing and Analysis for Design Evaluation and Monitoring of Heliostats, *Journal of Solar Energy Engineering 137 (4)*, pp.0210101-02101010, DOI: 10.1115/1.4028561

Holmes, J.D., Kwok, K.C.S. and Ginger, J.D., 2012, *Wind Loading Handbook for Australia and New Zealand: background to AS/NZS1170.2 wind actions*. AWES-HB-001-2012 . Australasian Wind Engineering Society, Sydney, NSW, Australia.

Huss, S., Traeger, Y.D., Shvets, Z.,Rojansky, M., Stoyanoff, S., Garber, J., 2011. Evaluating effects of wind loads in heliostat design. *SolarPACES 2011,* Granada, Spain.

Mammar, M., Djouimaa, S., Gärtner, U., Hamidat, A., 2018. Wind loads on heliostats of various column heights: An experimental study. *Energy 143,* pp. 867-880.

Manwell, J.F., McGowan, J.G., Rogers, A.L., 2009. *Wind Energy Explained – Theory, Design and Application*, 2nd Ed., John Wiley and Sons,

Matty, R., 1979. *Vortex shedding from square plates near a ground plane: An experimental study*, Texas Tech University: Masters in Mechanical Engineering.

Menter, F., 2015. *Best Practice: Scale-Resolving Simulations in ANSYS CFD V.2,* Germany: ANSYS Inc.

Peterka, J., Hosoya, N., Bienkiewicz, B., Cermak, J., 1986. *Wind load reduction for heliostats,* s.l.: Solar Energy Research Institute SERI.

Peterka, J., Bienkiewicz, B., Tan, Z., Cermak, J., 1989. Mean and Peak Wind Loads on Heliostats. *Journal of solar energy engineering 111(2),* pp. 158-164.

Peterka, J.A, Derickson, R.G., 1992. Wind load design methods for ground-based heliostats and parabolic dish collectors. *Sandia National Laboratories, SAND92-7009.* Albuquerque, NM.

Pfahl, A., Buselmeier, M., Zaschke, M., 2011. Wind loads on heliostats and photovoltaic trackers of various aspect ratios. *Solar Energy* 85, 2185-2201.

Pfahl, A., Uhlemann, P., 2011. Wind loads on heliostats and photovoltaic trackers at various Reynolds numbers. *Journal of Wind Engineering and Industrial Aerodynamics*99, 964-968.

Pfahl, A., Coventry, J., Röger, M., Wolfertstetter, F., Vasquez, F.,Gross, F., Arjomandi, M., Schwarzbözl, P., Geiger, M., Liedke, P., 2017. Progress in heliostat development. *Solar Energy 152,* pp. 3-37.

Poulain, P.E., Marais, M.D., Craig, K.J., Meyer, J.P., 2016. Using RANS-LES formulations in the CFD modeling of heliostat peak loads, 4th South African Solar Energy Conference, 31 October – 2 November 2016, Stellenbosch, South Africa.

Rebolo, R., Lata, J., Vázquez, 2011. Design of Heliostats Under Extreme and Fatigue Wind Loads, *SolarPACES 2011,* Granada, Spain.

Richards, P., Hoxey, R., 1993. Appropriate boundary conditions for computational wind engineering methods using the k-ε turbulence model. *Journal of Wind Engineering and Industrial Aerodynamics 46&47,* pp. 145-153.

Richards, P., Norris, S., 2011. Appropriate boundary conditions for computational wind engineering models revisited. *Journal of Wind Engineering and Industrial Aerodynamics 99(4),* pp. 257-266.

Sakamoto, H. and Arie, M., 1983, Vortex shedding from a rectangular prism and a circular cylinder placed vertically in a turbulent boundary layer, Journal of Fluid Mechanics 126, 147-165.

Sakamoto, H., Hainu, H. and Obata, Y., 1987, Fluctuating forces acting on two square prisms in a tandem arrangement, Journal of Wind Engineering and Industrial Aerodynamics 26, 85-103.

Sment, J., Ho, C., 2014. Wind patterns over a heliostat field. SolarPACES 2013, *Energy Procedia 49*, 229-238.

Sun, H., Gong, B., Yao, Q., 2014. A review of wind loads on heliostats and trough collectors. *Renewable and Sustainable Energy reviews 32*, 206-221.

Vásquez-Arango, J.F., 2016. *Dynamic Wind Loads on Heliostats*, PhD Thesis, DLR, Uni Aachen.

Vásquez-Arango, J.F., Buck, R., Pitz-Paal, R., 2015. Dynamic Properties of a Heliostat Structure Determined by Numerical and Experimental Modal Analysis, *Journal of Solar Energy Engineering 137 (5)*, pp.051001-051001. DOI:10.1115/1.4030846.

Yu, J.S., Arjomandi, M., Ghanadi, F. and Kelso, R.M., 2016, The Effect of Inclination Angle on the Flow Characteristics of Tandem Bluff Plates, In: Proc., 20th Australasian Fluid Mechanics Society Conference, Perth, Australia.